2022 Tonga volcanic eruption induced global propagation of ionospheric disturbances via Lamb waves

Shun-Rong Zhang[1,1], Juha Vierinen[2,2], Ercha Aa[1,1], Larisa Goncharenko[1,1], Phil Erickson[1], William Rideout[1,1], Anthea Coster[1,1], Andres Spicher[2,2], and Phil Erickson[1]

[1]MIT Haystack Observatory
[2]The Arctic University of Norway

November 30, 2022

Abstract

The Tonga volcano eruption at 04:14:45 UT on 2022-01-15 released enormous amounts of energy into the atmosphere, triggering very significant geophysical variations not only in the immediate proximity of the epicenter but also globally across the whole atmosphere. This study provides a global picture of ionospheric disturbances over an extended period for at least four days. We find traveling ionospheric disturbances (TIDs) radially outbound and inbound along entire Great-Circle loci at primary speeds of $\sim$300-350 m/s (depending on the propagation direction), going around the globe for three times, passing six times over the continental US in 100 hours since the eruption. These TIDs have a range of periods but predominately occur at 10-30 min. TID global propagation is consistent with the effect of Lamb waves which travel at the speed of sound. Although these oscillations are often confined to the troposphere, Lamb wave energy is known to leak into the thermosphere through channels of atmospheric resonance at acoustic and gravity wave frequencies, carrying substantial wave amplitudes at high altitudes. Prevailing Lamb waves have been reported in the literature as atmospheric responses to the gigantic Krakatoa eruption in 1883 and other geohazards. This study provides substantial first evidence of their long-duration imprints up in the global ionosphere. This study was enabled by ionospheric measurements from 5,000+ world-wide Global Navigation Satellite System (GNSS) ground receivers, demonstrating the broad implication of the ionosphere measurement as a sensitive detector for atmospheric waves and geophysical disturbances.

2022 Tonga volcanic eruption induced global propagation of ionospheric disturbances via Lamb waves

Shun-Rong Zhang [1,*], Juha Vierinen [2], Ercha Aa [1], Larisa P. Goncharenko [1], Philip J. Erickson [1], William Rideout [1], Anthea J. Coster [1], and Andres Spicher [2]

[1] *Haystack Observatory, Massachusetts Institute of Technology, Westford, MA, USA*
[2] *Department of Physics and Technology, The Arctic University of Norway, Tromsø, Norway*

Correspondence*:
Shun-Rong Zhang
shunrong@mit.edu

ABSTRACT

The Tonga volcano eruption at 04:14:45 UT on 2022-01-15 released enormous amounts of energy into the atmosphere, triggering very significant geophysical variations not only in the immediate proximity of the epicenter but also globally across the whole atmosphere. This study provides a global picture of ionospheric disturbances over an extended period for at least four days. We find traveling ionospheric disturbances (TIDs) radially outbound and inbound along entire Great-Circle loci at primary speeds of ∼300-350 m/s (depending on the propagation direction), going around the globe for three times, passing six times over the continental US in 100 hours since the eruption. These TIDs have a range of periods but predominately occur at 10-30 min. TID global propagation is consistent with the effect of Lamb waves which travel at the speed of sound. Although these oscillations are often confined to the troposphere, Lamb wave energy is known to leak into the thermosphere through channels of atmospheric resonance at acoustic and gravity wave frequencies, carrying substantial wave amplitudes at high altitudes. Prevailing Lamb waves have been reported in the literature as atmospheric responses to the gigantic Krakatoa eruption in 1883 and other geohazards. This study provides substantial first evidence of their long-duration imprints up in the global ionosphere. This study was enabled by ionospheric measurements from 5,000+ world-wide Global Navigation Satellite System (GNSS) ground receivers, demonstrating the broad implication of the ionosphere measurement as a sensitive detector for atmospheric waves and geophysical disturbances.

Keywords: Tonga volcano eruption, traveling ionospheric disturbances, Lamb waves, GNSS, Geohazard

1 INTRODUCTION

The Tonga volcano eruption at 04:14:45 UT on 2022-01-15 was a huge geohazard event with far-reaching effects, reportedly releasing 4-18 megatons of thermal energy (NASA website, 2022) and causing a range of geophysical disturbances (Duncombe, 2022). Previous events (e.g. Artru et al., 2005; Heki, 2006; Dautermann et al., 2009), and their effects in the charged upper atmosphere, are useful for comparison. The 1980 eruption of Mount St. Helens was a VEI (Volcanic Explosivity Index) 5 devastating disaster, comparable to the El Chichón eruption but less intense than the Pinatubo eruption at VEI 6. An estimated 24 megatons of energy release by this 1980 eruption (Kieffer, 1981) produced enormously impactful ionospheric disturbances at up to 9,000 km radius (Liu et al., 1982; Roberts et al., 1982). The reported ionospheric response to the Pinatubo eruption occurred at least 2,000-3,000 km distance across the Asian continent (Hao et al., 2006). Similar long distance effects occurred for the great Sumatra-Andaman earthquake (M 9.1 on Richter local magnitude scale) up to 5,000 km distance (Astafyeva and Afraimovich, 2006), and for the Tohuku earthquake (M 9.1) at up to 8,000-10,000 km distance in the US west coast (Crowley et al., 2016; Azeem et al., 2017).

Volcanic events can trigger severe disturbances that reach into the upper atmosphere above the epicenter, and in particular can produce periodic waves in both neutral and charged particles. A fundamental question for understanding the volcanic impact chain of response lies in characterization of the disturbance propagation mode in the upper atmosphere for given intensities of forcing and energy injection during the eruption. An eruption can excite both acoustic and infrasonic waves as compressional pressure waves, driving ionospheric plasma dynamics due to ion-neutral coupling. Tsunami waves are well known to be excited by the displacement of a large volume of water, and travel at a speed of $\sim$200 m/s for an ocean depth of $\sim$4000 km (e.g. Astafyeva, 2019, and references therein). Ocean-atmosphere interaction via tsunami waves can induce atmospheric gravity waves which lead to ionospheric disturbances (e.g. Artru et al., 2005). In aggregate, these various volcano driven wave modes are effective at causing ionospheric oscillations in the form of traveling ionospheric disturbances (TIDs) with periodicities spanning a few to 10s of min in the characteristic frequency domains of infrasonic, acoustic, tsunami, and gravity waves (e.g. Heki and Ping, 2005; Liu et al., 2006, 2010; Hao et al., 2012; Zhao and Hao, 2015; Galvan et al., 2012; Zettergren and Snively, 2015; Chum et al., 2018; Astafyeva, 2019, and references therein). Ionospheric observations provide an effective and unique means of detecting these waves, and other oscillations, occurring in the entire atmosphere.

The extreme Tonga eruption provides an unprecedented scientific opportunity to gauge the global impact of these class of events on the whole atmosphere, and to improve our fundamental understanding of atmospheric wave characteristics during vertical and horizontal propagation. Themens et al. (2022) provided the first examination of a portion of the global extent of the ionospheric responses to the eruption, and reported some common TID modes as described earlier. Our study focuses on several important new features of eruption ionospheric effects. These include radially two-way (full great-circles) disturbance propagation in the global ionosphere for 4 days, and the fundamental roles of atmospheric Lamb waves that likely drove observed TIDs. These waves are recognized for the first time to cause a global impact, well above their nominal dominant regime in the atmosphere.

2 METHOD AND DATA

We use GNSS total electron content (TEC) products from 5000+ worldwide GNSS (GPS, GLONASS, and Beidou) receivers, generated (Rideout and Coster, 2006; Vierinen et al., 2016) and provided via the Madrigal distributed data system developed at the Massachusetts Institute of Technology's Haystack Observatory. In order to detect ionospheric responses associated with the Tonga eruption, we calculated differential TEC using an approach that effectively removes the background ionospheric "trend", as used in many previous TID studies (Zhang et al., 2017, 2019a,b; Lyons et al., 2019; Sheng et al., 2020; Aa et al., 2021; England et al., 2021). Zhang et al. (2019a) provided more detailed discussions of this method. Differential TEC calculation of this nature is widely used for GNSS TEC based large and medium scale

TID and ionospheric disturbance studies (Saito et al., 1998; Tsugawa et al., 2007; Ding et al., 2007; Azeem et al., 2017; Chou et al., 2018; Astafyeva, 2019).

The analysis uses individual receiver-satellite TEC data segments, subtracting a background TEC variation determined, in our technique, by a low-pass filtering procedure using a Savitzky-Golay low-pass filter (Savitzky and Golay, 1964). This residual is also called differential TEC (dTEC). We use a 30-min sliding window and a linear basis function for this particular study. To be completely free from impacts of the data edge associated with the use of a 30-min fixed length window, we removed data for the first and the last 15-min of each data segment. Finally, our analysis disregarded any data with satellite elevation $< 15°$. Final accuracy of this method ultimately derives from the accuracy of the GNSS phase measurement. Assuming that there is no loss of phase lock in the receiver, the error in differential TEC is less than 0.03 TEC units (Coster et al., 2012), as all satellite and receiver bias terms cancel out in a differential sense.

3 RESULTS

3.1 Global extent of the disturbances

The Tonga eruption provided an equivalent point source for observed atmospheric disturbances. We evaluated these disturbances based on the great-circle distance from the epicenter location (-20.5°N, -175.4°E) as identified by the US Geological Survey for the eruption induced magnitude M 5.8 earthquake origin (USGS Website, 2022). Figure 1 provides relevant geometry information and great-circle distance contours from the eruption location, as well as a great circle oriented at 26 and 206° azimuth from the epicenter. Superimposed is a background global map of GNSS TEC measurements at three post-eruption instances. Great circles assume 300 km height, characteristic of approximate ionospheric F region altitudes near the peak of the plasma population. The maximum great-circle distance is located between southern Europe and northern Africa. New Zealand was 2-4,000 km away, central US 12,000 km, South Africa 14,000 km, and Europe 18,000 km. Upper atmospheric perturbations beyond 10,000 km have never been able to be examined before this eruption.

Both northern ($|\mathrm{Azimuth}| < 90°$) and southern (($|\mathrm{Azimuth}| > 90°$) great circles pass the polar latitudes. The great circle is presumed to be the shortest path along which disturbance energy and momentum in the neutral gas will flow radially from the epicenter. We note that, although global TEC is not evenly sampled by ground receivers with large gaps over the oceans, each observation is useful in distance-time analysis. Thus, in contrast to typical TEC studies, the distribution of disturbance propagation observations do not suffer severe gaps as demonstrated in the following distance-time figures. Themens et al. (2022) also presented these type of distance-time figures, and our analysis is similar except that we provide propagation estimates also based on azimuth bearing of great circles. The approach allows us to precisely locate propagation signatures and clearly identify inbound waves.

The distance-time variation of dTEC illustrated in Figure 2 indicate dramatic development of disturbance global propagation over a prolonged period. The southward propagation from Tonga to Africa sectors via the southern polar region shows a defined envelope, as marked by fiducial arrows bounding enhanced disturbance (in dTEC) as a function of distance and UT. The width of the envelopes is $\sim$ 8 hours in time with $\sim$350 m/s slopes. Results show that dTEC fluctuations reached the furthest distance at $\sim$20,000 km via the southern polar region. Northward propagation is predominately similar as indicated by envelope lines and their slopes, and also reached $\sim$20,000 km distance where it encountered the southern outbound propagation. Although dTEC signals became weak at several distances of 14,000 km and 16,000 km, corresponding to European sectors and mid latitudes, propagation signals reappeared beyond those distances perhaps due to wave modulation. In the following discussion, we examine detailed regional characteristics in near-field and far-field regions and provide further evidence of ionospheric perturbation arrivals.

3.2 Near-field ionospheric disturbances

GNSS TEC measurements indicate immediate and vast near-field Tonga event atmospheric perturbations as demonstrated in Themens et al. (2022) and Figure 3. The earliest response was a positive dTEC occurring within 200 km of the epicenter almost instantaneously following the eruption at ∼04:15UT. This response, with ∼1 km/s radial propagation for the first 20 min, was an indication of supersonic infrasonic waves typically seen (as Rayleigh waves) during earthquake events (see Astafyeva, 2019, and references therein). Immediately following, two enormous shocks occurred with dTEC magnitudes up to 3 TECu (1TECu = 10^{16} electrons/m^2). Radial propagation initially occurred at ∼700 m/s speed, gradually slowing down to ∼450 m/s, and reached ∼5,000 km distance. The initial waves were clearly identifiable over New Zealand between 0500-0645 UT (e.g., Figure 3) and, specifically, at ∼06:20 UT with 2-D fronts (Figure 1b). Subsequent waves were characterized by smaller amplitudes at lower and relatively stable speeds of ∼360 m/s. These fluctuations had ∼10-30 min quasi-periodicity for at least 8 hours (see Figures 3a,b,c, and also Figure 2). The 2-D wave fronts as shown in Figures 1a and c indicated horizontal wavelengths between 200-500 km.

3.3 Far-field ionospheric responses

Beyond the near-field, outbound ionospheric responses propagated into different regions of the world. Within 195-315°azimuth bearing of the great circles, the disturbance propagation signals were evident between 13-18,000 km (Figure 4a), particularly over South Africa, with large amplitudes and consistent ∼ 350 m/s propagation speeds. These disturbances lasted at least 5 hours with up to ∼10-30 min periods, arriving via southern great circles (Figure 1a). These results were derived as dTEC averages in time and distance with 1 minute bins size in time and 10 km bin size in distance. 2-D wavefronts showed well organized disturbances with ≥500 km wavelengths (Figure 4c).

The continental US (CONUS) has dense receiver networks, therefore only a narrow range of azimuths (55-58°) are taken into account, to minimize decoherence of the wave signature due to regional deviations in the group velocity of the wave fronts. Such deviations can be caused by e.g., prevailing wind velocity, atmospheric pressure, and propagation direction (Taylor, 1932). Figure 4b shows the first sign of disturbance arrival in the west coast (8-9,000 km distance) at ∼11-12:00 UT, and the earliest front departed off the east coast by ∼16:00 UT . Throughout, propagation speed remained at ∼350 m/s. Some samples of 2-D wavefronts are shown in Figure 4e. dTEC enhancements were aligned with iso-distance lines, and separated zonally by ∼300-500 km spacing (wavelengths). Simultaneously, background medium-scale TIDs were present, likely associated with recovery from a geospace storm with minimum Dst -94 nT at 23:00 UT on 2022-01-14 (according to Kyoto Geomagnetic Dst Data, 2022) and/or with gravity waves linked to the strong stratospheric polar vortex (Sato and Yoshiki, 2008; Becker and Vadas, 2018; Bossert et al., 2020). The arriving eruption-induced fluctuations segmented these pre-existing TIDs fronts (with large components in a zonal alignment) into smaller structures elongated along iso-distance lines.

3.4 Wave propagation return to Tonga

Ionospheric fluctuations continued to propagate through the eruption antipode in southern Europe toward Tonga on the next day. These returning TIDs were most evident over South Africa (Figure 4b) where the disturbance phase was clearly toward shorter distance (white arrows), starting at 03:00 UT at 15,000 km distance. The speed was ∼350 m/s. Figure 4e shows an example of wavefronts associated with the returning TIDs at 03:30 UT on 2022-01-16, close to local sunrise time. The timing of the returning TIDs is approximately consistent with propagation from the most distant point to South Africa along the great-circle Tonga – CONUS – Europe – South Africa – Tonga path (Figure 1a). Returning TIDs occurred also across the CONUS over a prolonged period initially at ∼0600 UT (see white arrows in Figure 4a), following a longer path of Tonga – southern high latitudes – South Africa – Europe – CONUS.

In the near field, clear indications occurred of the wave returning to New Zealand (Figure 3c) by ∼13:00 UT (or to Tonga by ∼15:00 UT), after traveling nearly 1.5 days along the complete great-circle. This timing is roughly consistent with a propagation at ∼350 m/s speed around the full great-circle.

3.5 Discussion

During the TID global propagation, the horizontal phase speed varied between 300-350 m/s depending on propagation direction. For example, Figure 2 marks a southward propagation (red arrow) at 300 m/s. However, these speed estimations are generally consistent with infrasonic detection of pressure wave arrival at individual stations around the world, e.g., in northern Europe (Norstar Website, 2022) using the network established to monitor compliance with the Comprehensive Nuclear Test Ban Treaty and over CONUS using the pressure altimeter observations (Iowa Environmental Mesonet, 2022). Lamb waves travel at the sound speed, typically 300-350 m/s in the troposphere, and can exist at any period. Although their energy is confined to the troposphere, their amplitudes increase exponentially with height due to decreasing density. Their wave energy can leak into the upper atmosphere when Lamb waves with ∼300 m/s horizontal phase speed are resonant with the atmosphere, as can be the case with acoustic and gravity waves (Bretherton, 1969; Lindzen and Blake, 1972; Nishida et al., 2014). Lamb waves with ∼319 m/s phase speed were previously identified as an atmospheric wave response to the Krakatoa eruption (Symons, 1888; Taylor, 1932). Similar Lamb waves were also detected by very sensitive microbarographs during the St. Helens eruption (Mikumo and Bolt, 1985) and the Sumatra-Andaman earthquake (Mikumo et al., 2008).

A significant portion of our GNSS observations occurred inland, where direct tsunami wave contribution to these TID results may be ignored. Furthermore, an additional argument against the presumption of tsunami wave presence with 10-30 min periodicity and 300-350 m/s travel speed as noted earlier: tsunami waves were reported to occur in the US west coast at 15:30-16:00 UT (NOAA DART and NOAA/NOS/CO-OPS Data, 2022) consistent with an anticipated 210-220 m/s propagation speed across the Pacific ocean. This is clearly different from observed ionospheric wave propagation which arrived at least ∼4 hours earlier than the tsunami waves in the US west coast. Nevertheless, continued community study is recommended to further clarify the roles of tsunami and gravity wave interactions and the factors that are potentially responsible for their different propagation speeds (Makela et al., 2011; Kherani et al., 2016; Bagiya et al., 2017).

The earliest wavefronts could be seen traveling around the globe three times, passing six times over the CONUS over 100 hrs since the eruption (Figures 4b,f; the pass 6 over CONUS occurred at ∼12:00 UT on 2022-01-19 but is not shown here due to the space limit). The travel time around the globe in the direction against Earth's rotation was 34.8 ± 0.7 hours and in the opposite direction 36.0 ± 0.7 hours. The error estimates are roughly one order of magnitude estimates based on visual inspection.The measured propagation speed and the number of observed passes of the atmospheric wave are comparable to those reported with the Krakatoa eruption (Symons, 1888). Time periods before and after the eruption were processed with the same analysis, and no similar traces corresponding to ones shown in Figures 4b,f were observed before the eruption.

4 SUMMARY

The 2021 Tonga volcano eruption caused enormous and truly global perturbations in the ionosphere and thermosphere over an extended period. Ionospheric disturbances were observed traveling three times around the globe. They returned back to Tonga every 1.5 days. The ionospheric responses were characterized by an immediate supersonic plasma density impulse, and two shock waves with substantial amplitudes in ≤5,000 km near-field regions including New Zealand to the south, and Hawaii to the north. Subsequently, persistent (lasting 8 hours) slow-propagating TIDs developed, most significantly in the near-field (<5,000 km radius). Far-field wave effects include TIDs whose spatial wavefronts were clearly organized based on the distance from Tonga in the continental US (∼12,000 km distances) and mid latitude west Europe (∼ 18,000 km distances), with the two destination regions connected via the northern polar region along the great circle with an origin in Tonga. A similar path of global wave propagation occurred in the southern hemisphere along a New Zealand - southern polar region - South Africa route.

These disturbances resulted from eruption-induced perturbations at frequencies of acoustic waves (including Lamb waves) and gravity waves. Eruption-associated tsunami waves were slower than the main component of ionospheric waves that propagated globally and are therefore unlikely responsible for the TID global propagation. The presumption of Lamb wave global propagation at 300-350 m/s is consistent with our main observational results. These waves provide one of the main carriers for eruption energy leaking into the upper atmosphere because of atmospheric resonance to forcing provided by these waves at ∼300 m/s phase speed, equivalent to the speed of sound in the troposphere. These ionospheric propagation results are also consistent with data from infrasonic global detections and other pressure wave detections. Our multi-sensor investigation, based on 5000+ world-wide GNSS receivers, reveals the unprecedented depth, severity, and extent of disturbances in the whole atmosphere in vertical and horizontal dimensions that occur during an extremely devastating geohazard impact. This is yet another demonstration of the ionosphere acting as a sensitive detector for atmospheric waves.

CONFLICT OF INTEREST STATEMENT

The authors declare that the research was conducted in the absence of any commercial or financial relationships that could be construed as a potential conflict of interest.

AUTHOR CONTRIBUTIONS

SRZ was responsible for differential TEC derivation, science analysis of the observational results, preparing the initial manuscript and organizing team efforts. JV contributed initial figures for comparisons, science analysis, discussion, and organizing team research. EA was responsible for Beidou GNSS data processing. LPG conducted analysis of TIDs that could potentially be linked to meteorological disturbances. PJE contributed substantially manuscript development. AJC was responsible for GNSS data management. WR was responsible for software development of GNSS data processing and daily GNSS data processing. AS contributed examining satellite data. All members contributed to science discussion and manuscript development.

FUNDING

GNSS TEC data products and access through the Madrigal distributed data system are provided to the community by the Massachusetts Institute of Technology under support from US National

Science Foundation grant AGS-1952737. MIT staff members were partially supported by NASA grants 80NSSC21K1775 and 80NSSC21K1310, AFOSR MURI grant FA9559-16-1-0364, NSF grant AGS-2033787 and ONR grant N00014-17-1-2186.

ACKNOWLEDGMENTS

Data for TEC processing is provided from the following organizations: UNAVCO, Scripps Orbit and Permanent Array Center, Institut Geographique National, France, International GNSS Service, The Crustal Dynamics Data Information System (CDDIS), National Geodetic Survey, Instituto Brasileiro de Geografia e Estatística, RAMSAC CORS of Instituto Geográfico Nacional de la República Argentina, Arecibo Observatory, Low-Latitude Ionospheric Sensor Network (LISN), Topcon Positioning Systems, Inc., Canadian High Arctic Ionospheric Network, Institute of Geology and Geophysics, Chinese Academy of Sciences, China Meteorology Administration, Centro di Ricerche Sismologiche, Système d'Observation du Niveau des Eaux Littorales (SONEL), RENAG : REseau NAtional GPS permanent, GeoNet - the official source of geological hazard information for New Zealand, GNSS Reference Networks, Finnish Meteorological Institute, and SWEPOS - Sweden.

DATA AVAILABILITY STATEMENT

GNSS TEC data products and access through the Madrigal distributed data system [http://openmadrigal.org] are provided to the community by the Massachusetts Institute of Technology. The datasets generated for this study can be found in the here.

REFERENCES

Aa, E., Zhang, S.-R., Erickson, P. J., Coster, A. J., Goncharenko, L. P., Varney, R. H., et al. (2021). Salient Midlatitude Ionosphere-Thermosphere Disturbances Associated With SAPS During a Minor but Geo-Effective Storm at Deep Solar Minimum. *Journal of Geophysical Research: Space Physics* 126, e2021JA029509

Artru, J., Ducic, V., Kanamori, H., Lognonné, P., and Murakami, M. (2005). Ionospheric detection of gravity waves induced by tsunamis. *Geophysical Journal International* 160, 840–848. doi:10.1111/j.1365-246X.2005.02552.x

Astafyeva, E. (2019). Ionospheric Detection of Natural Hazards. *Reviews of Geophysics* 3, 673

Astafyeva, E. I. and Afraimovich, E. L. (2006). Long-distance traveling ionospheric disturbances caused by the great Sumatra-Andaman earthquake on 26 December 2004. *Earth, Planets and Space* 58, 1025–1031

Azeem, I., Vadas, S. L., Crowley, G., and Makela, J. J. (2017). Traveling ionospheric disturbances over the United States induced by gravity waves from the 2011 Tohoku tsunami and comparison with gravity wave dissipative theory. *Journal of Geophysical Research: Space Physics* 122, 3430–3447

Bagiya, M. S., Kherani, E., Sunil, P., Sunil, A., Sunda, S., and Ramesh, D. (2017). Origin of the ahead of tsunami traveling ionospheric disturbances during Sumatra tsunami and offshore forecasting. *Journal of Geophysical Research: Space Physics* 122, 7742–7749

Becker, E. and Vadas, S. L. (2018). Secondary gravity waves in the winter mesosphere: Results from a high-resolution global circulation model. *Journal of Geophysical Research: Atmospheres* 123, 2605–2627

Bossert, K., Vadas, S. L., Hoffmann, L., Becker, E., Harvey, V. L., and Bramberger, M. (2020). Observations of stratospheric gravity waves over europe on 12 january 2016: The role of the polar night jet. *Journal of Geophysical Research: Atmospheres* 125, e2020JD032893

Bretherton, F. (1969). Lamb waves in a nearly isothermal atmosphere. *Quarterly Journal of the Royal Meteorological Society* 95, 754–757

Chou, M.-Y., Lin, C. C. H., Shen, M.-H., Yue, J., Huba, J. D., and Chen, C.-H. (2018). Ionospheric disturbances triggered by SpaceX Falcon Heavy. *Geophysical Research Letters* 45, 6334–6342. doi:10.1029/2018GL078088

Chum, J., Liu, J. Y., Podolská, K., and Šindelářová, T. (2018). Infrasound in the ionosphere from earthquakes and typhoons. *Journal of Atmospheric and Solar-Terrestrial Physics* 171, 72–82

Coster, A., Herne, D., Erickson, P., and Oberoi, D. (2012). Using the Murchison Widefield Array to observe midlatitude space weather. *Radio Science* 47, RS0K07. doi:10.1029/2012RS004993

Crowley, G., Azeem, I., Reynolds, A., Duly, T. M., McBride, P., Winkler, C., et al. (2016). Analysis of traveling ionospheric disturbances (TIDs) in GPS TEC launched by the 2011 Tohoku earthquake. *Radio Science* 51, 507–514

Dautermann, T., Calais, E., and Mattioli, G. S. (2009). Global positioning system detection and energy estimation of the ionospheric wave caused by the 13 july 2003 explosion of the soufrière hills volcano, montserrat. *Journal of Geophysical Research: Solid Earth* 114. doi:https://doi.org/10.1029/2008JB005722

Ding, F., Wan, W., Ning, B., and Wang, M. (2007). Large-scale traveling ionospheric disturbances observed by GPS total electron content during the magnetic storm of 29-30 October 2003. *Journal of Geophysical Research (Space Physics)* 112, A06309. doi:10.1029/2006JA012013

Duncombe, J. (2022). The surprising reach of Tonga's giant atmospheric waves. *Eos: AGU Science News* 103

England, S. L., Greer, K. R., Zhang, S.-R., Evans, S., Solomon, S. C., Eastes, R. W., et al. (2021). First comparison of travelling atmospheric disturbances observed in the middle thermosphere by GOLD to travelling ionospheric disturbances seen in ground-based total electron content observations. *Journal of Geophysical Research: Space Physics* , e2021JA029248

Galvan, D. A., Komjathy, A., Hickey, M. P., Stephens, P., Snively, J., Song, Y. T., et al. (2012). Ionospheric signatures of Tohoku-Oki tsunami of March 11, 2011: Model comparisons near the epicenter. *Radio Science* 47, 1–10

Hao, Y., Xiao, Z., and Zhang, D. (2012). Multi-instrument observation on co-seismic ionospheric effects after great Tohoku earthquake. *Journal of Geophysical Research: Space Physics* 117

Hao, Y.-Q., Xiao, Z., and Zhang, D.-H. (2006). Responses of the Ionosphere to the Great Sumatra Earthquake and Volcanic Eruption of Pinatubo. *Chinese Physics Letters* 23, 1955

Heki, K. (2006). Explosion energy of the 2004 eruption of the asama volcano, central japan, inferred from ionospheric disturbances. *Geophysical Research Letters* 33. doi:https://doi.org/10.1029/2006GL026249

Heki, K. and Ping, J. (2005). Directivity and apparent velocity of the coseismic ionospheric disturbances observed with a dense GPS array. *Earth and Planetary Science Letters* 236, 845–855

[Dataset] Iowa Environmental Mesonet (2022). Pressure altimeter data movies: Past IEM Features tagged: Tonga. `https://mesonet.agron.iastate.edu/onsite/features/tags/tonga.html`. [Online; accessed 3-Feb-2022]

Kherani, E., Rolland, L., Lognonné, P., Sladen, A., Klausner, V., and de Paula, E. (2016). Traveling ionospheric disturbances propagating ahead of the Tohoku-Oki tsunami: a case study. *Geophysical Journal International* 204, 1148–1158

Kieffer, S. W. (1981). Blast dynamics at mount St Helens on 18 May 1980. *Nature* 291, 568–570

[Dataset] Kyoto Geomagnetic Dst Data (2022). Real-time Dst Index. `http://wdc.kugi.kyoto-u.ac.jp/dst_realtime/202201/index.html`. [Online; accessed 3-Feb-2022]

Lindzen, R. S. and Blake, D. (1972). Lamb waves in the presence of realistic distributions of temperature and dissipation. *Journal of Geophysical Research: Space Physics (1978–2012)* 77, 2166–2176

Liu, C. H., Klostermeyer, J., Yeh, K. C., Jones, T. B., Robinson, T., Holt, O., et al. (1982). Global dynamic responses of the atmosphere to the eruption of Mount St. Helens on May 18, 1980. *Journal of Geophysical Research: Space Physics (1978–2012)* 87, 6281–6290

Liu, J., Tsai, H., Lin, C., Kamogawa, M., Chen, Y., Lin, C., et al. (2010). Coseismic ionospheric disturbances triggered by the Chi-Chi earthquake. *Journal of Geophysical Research: Space Physics* 115

Liu, J., Tsai, Y., Chen, S., Lee, C., Chen, Y., Yen, H., et al. (2006). Giant ionospheric disturbances excited by the M9.3 Sumatra earthquake of 26 December 2004. *Geophysical Research Letters* 33

Lyons, L. R., Nishimura, Y., Zhang, S.-R., Coster, A. J., Bhatt, A., Kendall, E., et al. (2019). Identification of auroral zone activity driving large-scale traveling ionospheric disturbances. *Journal of Geophysical Research: Space Physics*

Makela, J., Lognonné, P., Hébert, H., Gehrels, T., Rolland, L., Allgeyer, S., et al. (2011). Imaging and modeling the ionospheric airglow response over Hawaii to the tsunami generated by the Tohoku earthquake of 11 March 2011. *Geophysical Research Letters* 38

Mikumo, T. and Bolt, B. A. (1985). Excitation mechanism of atmospheric pressure waves from the 1980 Mount St Helens eruption. *Geophysical Journal International* 81, 445–461

Mikumo, T., Shibutani, T., Le Pichon, A., Garces, M., Fee, D., Tsuyuki, T., et al. (2008). Low-frequency acoustic-gravity waves from coseismic vertical deformation associated with the 2004 Sumatra-Andaman earthquake (Mw=9.2). *Journal of Geophysical Research: Solid Earth* 113

[Dataset] NASA website (2022). Dramatic Changes at Hunga Tonga-Hunga Ha‘apai. [Online; accessed 3-Feb 2022]

Nishida, K., Kobayashi, N., and Fukao, Y. (2014). Background Lamb waves in the Earth's atmosphere. *Geophysical Journal International* 196, 312–316

[Dataset] NOAA DART and NOAA/NOS/CO-OPS Data (2022). January 15, 2022 Tonga Tsunami. `https://www.ngdc.noaa.gov/hazard/dart/2022tonga.html`. [Online; accessed 3-Feb-2022]

[Dataset] Norstar Website (2022). Enorm trykkbølge registrert etter vulkaneksplosjonen på Tonga. `https://www.norsar.no/i-fokus/enorm-trykkbolge-registrert-etter-vulkaneksplosjonen-pa-tonga`. [Online; accessed 3-Feb-2022]

Rideout, W. and Coster, A. (2006). Automated GPS processing for global total electron content data. *GPS Solutions* 10, 219–228

Roberts, D. H., Klobuchar, J. A., Fougere, P. F., and Hendrickson, D. H. (1982). A large-amplitude traveling ionospheric disturbance produced by the May 18, 1980, explosion of Mount St. Helens. *Journal of Geophysical Research: Space Physics (1978–2012)* 87, 6291–6301

Saito, A., Fukao, S., and Miyazaki, S. (1998). High resolution mapping of TEC perturbations with the GSI GPS Network over Japan. *Geophysical Research Letters* 25, 3079–3082. doi:10.1029/98GL52361

Sato, K. and Yoshiki, M. (2008). Gravity wave generation around the polar vortex in the stratosphere revealed by 3-hourly radiosonde observations at syowa station. *Journal of the Atmospheric Sciences* 65, 3719–3735

Savitzky, A. and Golay, M. J. E. (1964). Smoothing and differentiation of data by simplified least squares procedures. *Analytical Chemistry* 36, 1627–1639

Sheng, C., Deng, Y., Zhang, S.-R., Nishimura, Y., and Lyons, L. R. (2020). Relative Contributions of Ion Convection and Particle Precipitation to Exciting Large-Scale Traveling Atmospheric and Ionospheric Disturbances. *Journal of Geophysical Research: Space Physics* 125, 1667

Symons, G. J. (1888). *The Eruption of Krakatoa, and Subsequent Phenomena: Report of the Krakatoa Committee of the Royal Society* (Wiley Online Library)

Taylor, G. I. (1932). The resonance theory of semidiurnal atmospheric oscillations. *Roy. Meteorol. Soc.* 4[9], 41–52

Themens, D. R., Watson, C., Žagar, N., Vasylkevych, S., Elvidge, S., Mccaffrey, A., et al. (2022). Global propagation of ionospheric disturbances associated with the 2022 Tonga Volcanic Eruption. *Earth and Space Science Open Archive* , 25doi:10.1002/essoar.10510350.1

Tsugawa, T., Otsuka, Y., Coster, A. J., and Saito, A. (2007). Medium-scale traveling ionospheric disturbances detected with dense and wide TEC maps over North America. *Geophysical Research Letters* 34, L22101. doi:10.1029/2007GL031663

[Dataset] USGS Website (2022). M 5.8 Volcanic Eruption - 68 km NNW of Nuku‘alofa, Tonga. `https://earthquake.usgs.gov/earthquakes/eventpage/us7000gc8r/origin/detail`. [Online; accessed 3-Feb-2022]

Vierinen, J., Coster, A. J., Rideout, W. C., Erickson, P. J., and Norberg, J. (2016). Statistical framework for estimating GNSS bias. *Atmospheric Measurement Techniques* 9, 1303–1312. doi:10.5194/amt-9-1303-2016

Zettergren, M. D. and Snively, J. B. (2015). Ionospheric response to infrasonic-acoustic waves generated by natural hazard events. *Journal of Geophysical Research: Space Physics* 120, 8002–8024

Zhang, S.-R., Coster, A. J., Erickson, P. J., Goncharenko, L. P., Rideout, W., and Vierinen, J. (2019a). Traveling Ionospheric Disturbances and Ionospheric Perturbations Associated With Solar Flares in September 2017. *Journal of Geophysical Research: Space Physics* 60, 895

Zhang, S.-R., Erickson, P. J., Coster, A. J., Rideout, W., Vierinen, J., Jonah, O., et al. (2019b). Subauroral and polar traveling ionospheric disturbances during the 7-9 September 2017 storms. *Space Weather* , 2019SW002325

Zhang, S.-R., Erickson, P. J., Goncharenko, L. P., Coster, A. J., Rideout, W., and Vierinen, J. (2017). Ionospheric bow waves and perturbations induced by the 21 August 2017 solar eclipse. *Geophyical Research Letters* 44, 12,067–12,073

Zhao, B. and Hao, Y. (2015). Ionospheric and geomagnetic disturbances caused by the 2008 wenchuan earthquake: A revisit. *Journal of Geophysical Research: Space Physics* 120, 5758–5777

FIGURE CAPTIONS

Figure 1 Geometry information of Tonga eruption impact distance (green lines) determined based on the the great circle at 300 km (white or yellow lines) that connect to the eruption region. Iso-distance lines up to 20,000 km are separated at 20,000 km interval. Great circles start at the Tonga epicenter for azimuth 26/206°. Background colors are differential TEC measured from ground-based receivers to GPS, GLONASS and Beidou navigation systems for the early stage of upper atmospheric responses at 0830 UT (a), 0620 UT (b), and 0920 UT (c). TID wave fronts are annotated by red and blue arrows in the three maps.

Figure 2 Distance-UT variation of dTEC for disturbance propagation southward (negative distance) and northward (positive distance) along the great circle paths at 300 km altitude on 15 Jan. White arrows provide envelope lines encompassing the ionospheric disturbances. The slopes of these lines are ∼350 m/s. Dashed lines with larger slopes (∼700m/s) follow the initial ionospheric shocks which terminated after 5,000-6,000 km. Red arrows marks the radial propagation in the European sector which is zoomed out in Figure 4b.

Figure 3 Near-field observations of initial and subsequent GNSS TEC fluctuations: the time-distance (regardless direction) variation within 5,000 km 6 hours following the eruption (a); regional GNSS TEC fluctuations in New Zealand showing the evolution of fluctuation periodicities in space and time (b); near-field TIDs over 48 hours with some indications of the returning ionospheric fluctuations into Tonga on after 15:00 UT on the following 16 Jan (c) where red arrows with 350 m/s slope marked wave propagation and black arrows marked the returning TIDs.

Figure 4 Far-field ionospheric disturbances in selected regions: time-distance variation over Europe-Africa sectors with 195-315°azimuth bearing (a) and the continental US (CONUS) (b) over 48 hours between 2022-01-15∼16. Red solid lines and arrows mark the radial propagation for outbound waves, at ∼350 m/s (slope); white lines and arrows show the inbound waves toward Tonga on 2022-01-16. (c-d) show TID wavefronts over South Africa corresponding to (a) at 17:00 UT (outbound) and 03:30 UT (inbound). (e) shows TID wavefronts at 13:38 UT over CONUS corresponding to (b), Arrows in (c-e) indicate the radial outbound and inbound propagation along the great circles (marked by white dotted lines). (f) Same as (b) but for 2022-01-17∼18.

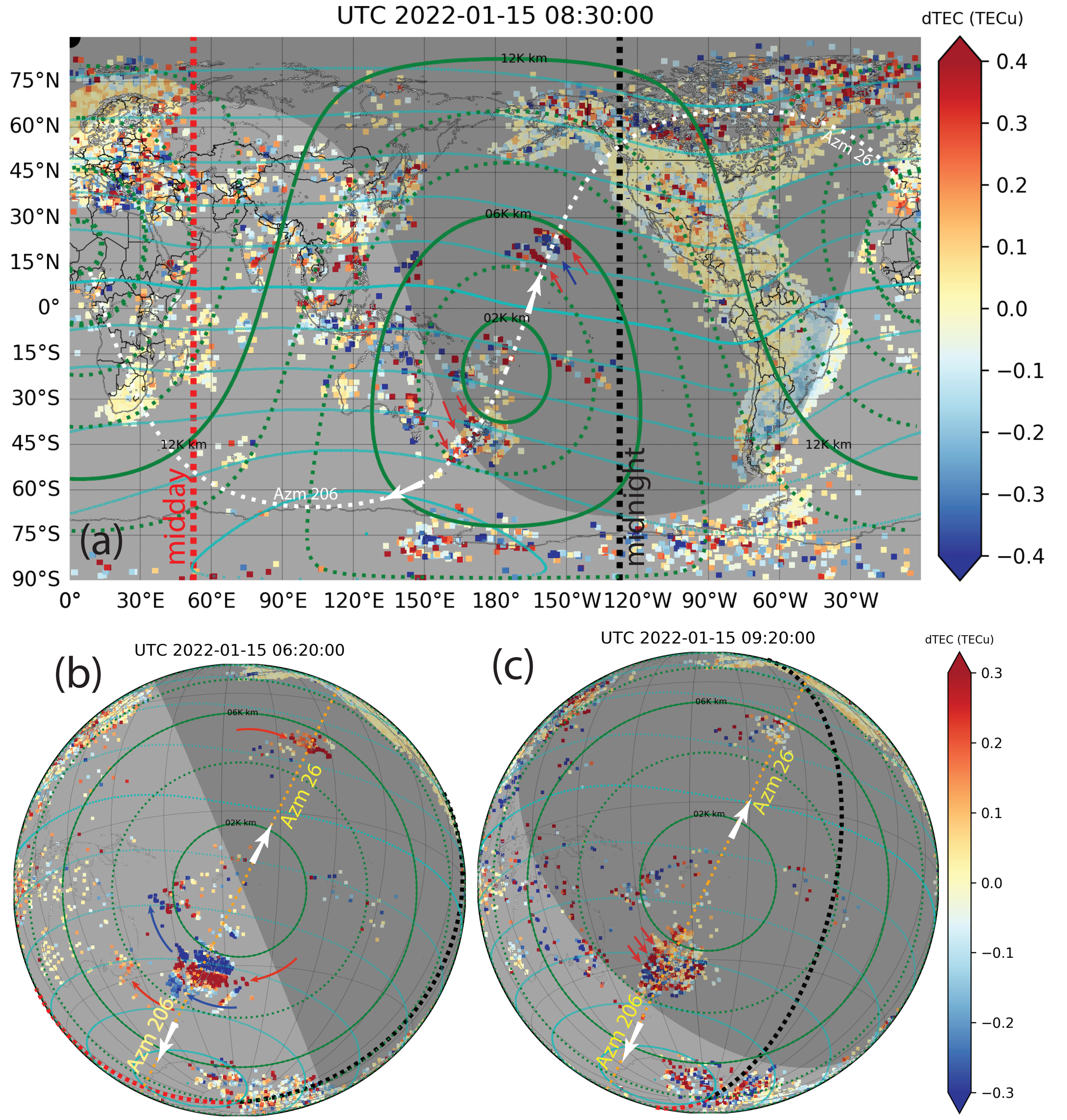

Figure 1. Geometry information of Tonga eruption impact distance (green lines) determined based on the the great circle at 300 km (white or yellow lines) that connect to the eruption region. Iso-distance lines up to 20,000 km are separated at 20,000 km interval. Great circles start at the Tonga epicenter for azimuth 26/206°. Background colors are differential TEC measured from ground-based receivers to GPS, GLONASS and Beidou navigation systems for the early stage of upper atmospheric responses at 0830 UT (a), 0620 UT (b), and 0920 UT (c). TID wave fronts are annotated by red and blue arrows in the three maps.

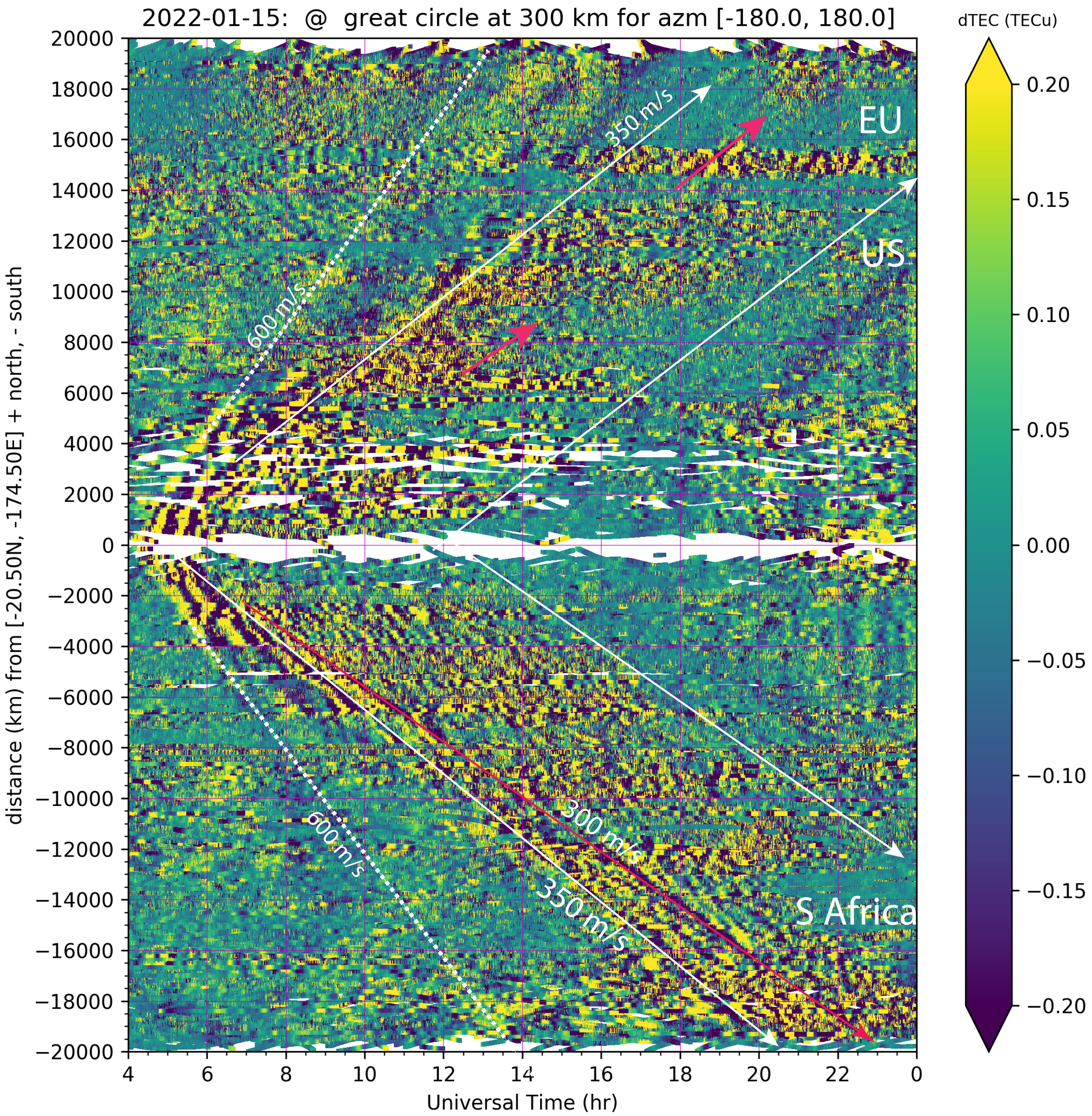

Figure 2. Distance-UT variation of dTEC for disturbance propagation southward (negative distance) and northward (positive distance) along the great circle paths at 300 km altitude on 15 Jan. White arrows provide envelope lines encompassing the ionospheric disturbances. The slopes of these lines are ∼350 m/s. Dashed lines with larger slopes (∼700m/s) follow the initial ionospheric shocks which terminated after 5,000-6,000 km. Red arrows marks the radial propagation in the European sector which is zoomed out in Figure 4b.

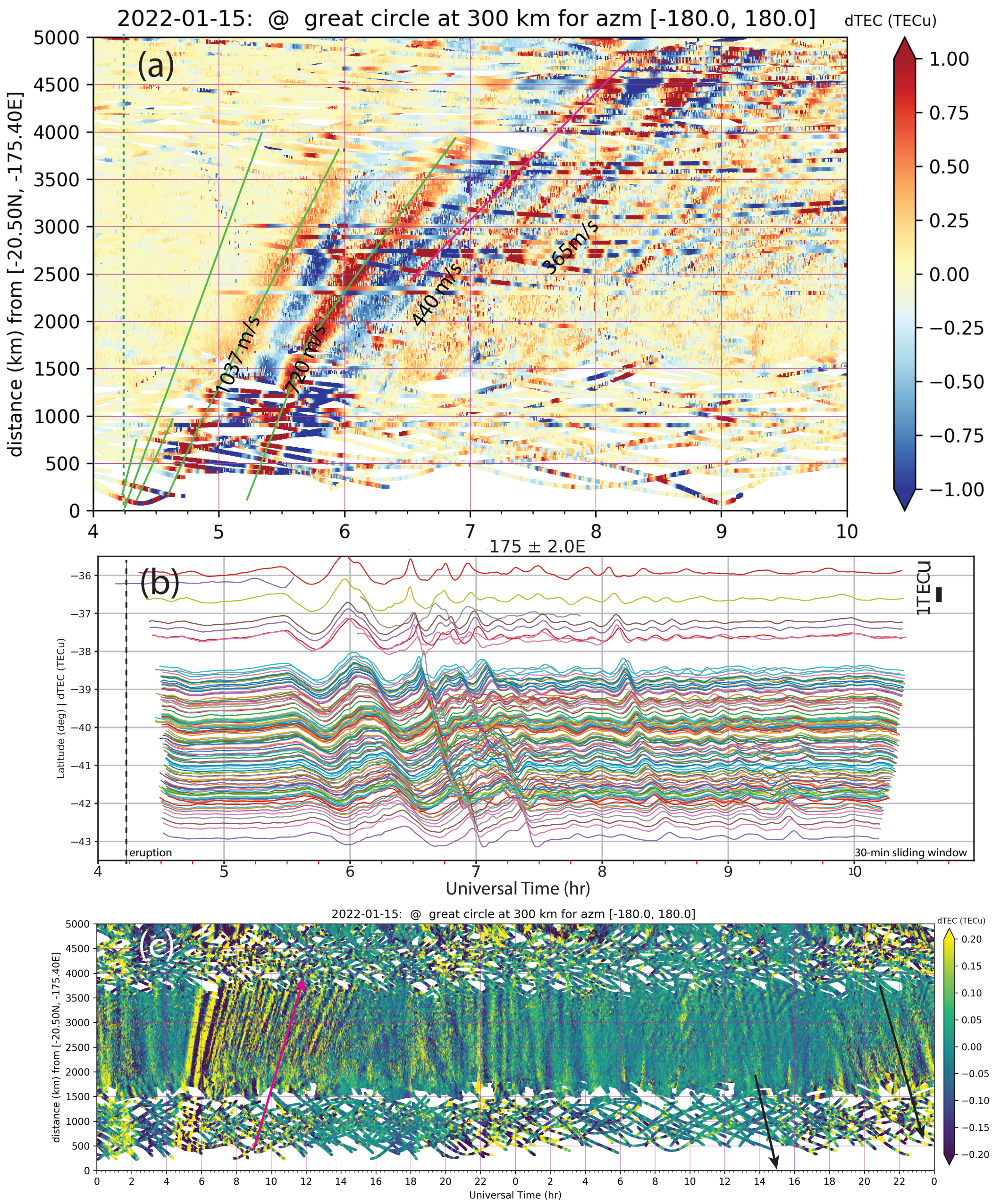

Figure 3. Near-field observations of initial and subsequent GNSS TEC fluctuations: the time-distance (regardless direction) variation within 5,000 km 6 hours following the eruption (a); regional GNSS TEC fluctuations in New Zealand showing the evolution of fluctuation periodicities in space and time (b); near-field TIDs over 48 hours with some indications of the returning ionospheric fluctuations into Tonga on after 15:00 UT on the following 16 Jan (c) where red arrows with 350 m/s slope marked wave propagation and black arrows marked the returning TIDs.

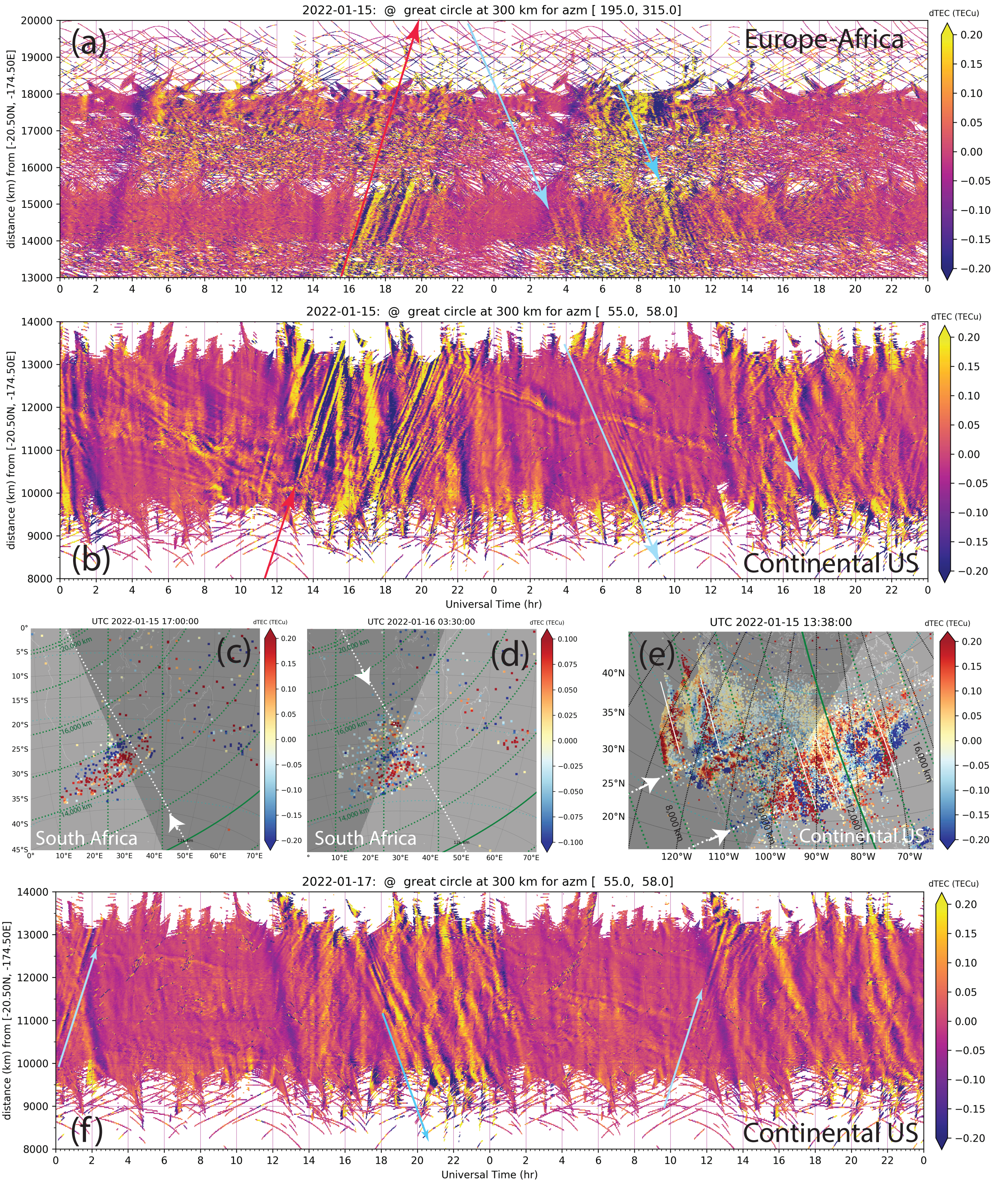

Figure 4. Far-field ionospheric disturbances in selected regions: time-distance variation over Europe-Africa sectors with 195-315°azimuth bearing (a) and the continental US (CONUS) (b) over 48 hours between 2022-01-15∼16. Red solid lines and arrows mark the radial propagation for outbound waves, at ∼350 m/s (slope); white lines and arrows show the inbound waves toward Tonga on 2022-01-16. (c-d) show TID wavefronts over South Africa corresponding to (a) at 17:00 UT (outbound) and 03:30 UT (inbound). (e) shows TID wavefronts at 13:38 UT over CONUS corresponding to (b), Arrows in (c-e) indicate the radial outbound and inbound propagation along the great circles (marked by white dotted lines). (f) Same as (b) but for 2022-01-17∼18.

Zhang et al. (2022) 2022 Tonga volcanic eruption induced global propagation of ionospheric disturbances via Lamb waves, *Frontier in Astronomy and Space Sciences*, DOI: 10.3389/fspas.2022.871275, in press

2022 Tonga volcanic eruption induced global propagation of ionospheric disturbances via Lamb waves

Shun-Rong Zhang [1,*], Juha Vierinen [2], Ercha Aa [1], Larisa P. Goncharenko [1], Philip J. Erickson [1], William Rideout [1], Anthea J. Coster [1], and Andres Spicher [2]

[1] *Haystack Observatory, Massachusetts Institute of Technology, Westford, MA, USA*
[2] *Department of Physics and Technology, The Arctic University of Norway, Tromsø, Norway*

Correspondence*:
Shun-Rong Zhang
shunrong@mit.edu

ABSTRACT

The Tonga volcano eruption at 04:14:45 UT on 2022-01-15 released enormous amounts of energy into the atmosphere, triggering very significant geophysical variations not only in the immediate proximity of the epicenter but also globally across the whole atmosphere. This study provides a global picture of ionospheric disturbances over an extended period for at least four days. We find traveling ionospheric disturbances (TIDs) radially outbound and inbound along entire Great-Circle loci at primary speeds of ∼300-350 m/s (depending on the propagation direction) and 500-1000 km horizontal wavelength for front shocks, going around the globe for three times, passing six times over the continental US in 100 hours since the eruption. TIDs following the shock fronts developed for ∼8 hours with 10-30 min predominant periods in near- and far- fields. TID global propagation is consistent with the effect of Lamb waves which travel at the speed of sound. Although these oscillations are often confined to the troposphere, Lamb wave energy is known to leak into the thermosphere through channels of atmospheric resonance at acoustic and gravity wave frequencies, carrying substantial wave amplitudes at high altitudes. Prevailing Lamb waves have been reported in the literature as atmospheric responses to the gigantic Krakatoa eruption in 1883 and other geohazards. This study provides substantial first evidence of their long-duration imprints up in the global ionosphere. This study was enabled by ionospheric measurements from 5,000+ world-wide Global Navigation Satellite System (GNSS) ground receivers, demonstrating the broad implication of the ionosphere measurement as a sensitive detector for atmospheric waves and geophysical disturbances.

Keywords: Tonga volcano eruption, traveling ionospheric disturbances, Lamb waves, GNSS, Geohazard

1 INTRODUCTION

The Tonga volcano eruption at 04:14:45 UT on 2022-01-15 was a huge geohazard event with far-reaching effects, reportedly releasing 4–18 megatons (16–75$\times10^{15}$J) of thermal energy (Garvin, 2022) and causing a range of geophysical disturbances (Duncombe, 2022). Previous events and their effects in the charged upper atmosphere (e.g. Artru et al., 2005; Heki, 2006; Dautermann et al., 2009) are useful for comparison.

The 1980 eruption of Mount Saint Helens was a VEI 5 (Volcanic Explosivity Index, see Newhall and Self, 1982) devastating disaster, comparable to the El Chichón eruption but less intense than the Pinatubo eruption at VEI 6. An estimated 24 megatons of energy release by this 1980 eruption (Kieffer, 1981) produced enormously impactful ionospheric disturbances at up to 9,000 km radius (Liu et al., 1982; Roberts et al., 1982). The reported ionospheric response to the Pinatubo eruption occurred at least 2,000-3,000 km distance across the Asian continent (Hao et al., 2006). Similar long distance effects occurred for the great Sumatra-Andaman earthquake (M 9.1 on Richter local magnitude scale) up to 5,000 km distance (Astafyeva and Afraimovich, 2006), and for the Tohuku earthquake (M 9.1) at up to 8,000-10,000 km distance in the US west coast (Crowley et al., 2016; Azeem et al., 2017).

Volcanic events can trigger severe disturbances that reach into the upper atmosphere above the epicenter, and in particular can produce periodic waves in both neutral and charged particles. A fundamental question for understanding the volcanic impact chain of response lies in characterization of the disturbance propagation mode in the upper atmosphere for given intensities of forcing and energy injection during the eruption. An eruption can excite both acoustic and infrasonic waves as compressional pressure waves, driving ionospheric plasma dynamics due to ion-neutral coupling. Tsunami waves are well known to be excited by the displacement of a large volume of water, and travel at a speed of $\sim$200 m/s for an ocean depth of $\sim$4000 km (e.g. Astafyeva, 2019, and references therein). Ocean-atmosphere interaction via tsunami waves can induce atmospheric gravity waves which lead to ionospheric disturbances (e.g. Artru et al., 2005). In aggregate, these various volcano driven atmospheric wave modes are effective at causing ionospheric oscillations in the form of traveling ionospheric disturbances (TIDs) with periodicities spanning a few to 10s of min in the characteristic frequency domains of infrasonic, acoustic, tsunami, and gravity waves (e.g. Heki and Ping, 2005; Liu et al., 2006, 2010; Hao et al., 2012; Zhao and Hao, 2015; Galvan et al., 2012; Zettergren and Snively, 2015; Chum et al., 2018; Astafyeva, 2019, and references therein). Ionospheric observations provide an effective and unique means of detecting these waves, and other oscillations, occurring in the entire atmosphere.

The extreme Tonga eruption provides an unprecedented scientific opportunity to gauge the global impact of this class of geohazard events on the whole atmosphere, and to improve our fundamental understanding of atmospheric wave characteristics during vertical and horizontal propagation. Themens et al. (2022) provided the first examination of a portion of the global extent of the ionospheric responses to the eruption, and reported some common TID modes as described earlier. Our study focuses on several important new features of eruption ionospheric effects. These include radially two-way (along full great-circles) disturbance propagation in the global ionosphere for 4 days, and the fundamental roles of atmospheric Lamb waves that likely drove observed TIDs. These waves are recognized for the first time to cause a global impact over an extended period, well above their nominal dominant regime in the atmosphere.

2 METHOD AND DATA

We use GNSS total electron content (TEC) products from 5000+ worldwide GNSS (GPS, GLONASS, and Beidou) receivers, generated (Rideout and Coster, 2006; Vierinen et al., 2016) and provided via the Madrigal distributed data system developed at the Massachusetts Institute of Technology's Haystack Observatory. In order to detect ionospheric responses associated with the Tonga eruption, we calculated differential TEC using an approach that effectively removes the background ionospheric "trend", as used in many previous TID studies (Zhang et al., 2017, 2019a,b; Lyons et al., 2019; Sheng et al., 2020; Aa et al., 2021; England et al., 2021). Zhang et al. (2019a) provided more detailed discussions of this method. Differential TEC calculation of this nature is widely used for GNSS TEC based large and medium scale TID and ionospheric disturbance studies (Saito et al., 1998; Tsugawa et al., 2007; Ding et al., 2007; Komjathy et al., 2016; Zakharenkova et al., 2016; Azeem et al., 2017; Chou et al., 2018; Astafyeva, 2019).

The analysis uses individual receiver-satellite TEC data segments, subtracting a background TEC variation determined, in our technique, by a low-pass filtering procedure using a Savitzky-Golay low-pass filter (Savitzky and Golay, 1964). This residual is also called differential TEC (dTEC). We use a 30-min sliding window and a linear basis function for this particular study. To be completely free from impacts of the data edge associated with the use of a 30-min fixed length window, we removed data for the first and the last 15-min of each data segment. Finally, our analysis disregarded any data with satellite elevation $< 15°$. Final accuracy of this method ultimately derives from the accuracy of the GNSS phase measurement. Assuming that there is no loss of phase lock in the receiver, the error in differential TEC is less than 0.03 TEC units (Coster et al., 2012), as all satellite and receiver bias terms cancel out in a differential sense.

3 RESULTS

3.1 Global extent of the disturbances

The Tonga eruption provided an equivalent point source for observed atmospheric disturbances. We evaluated these disturbances based on the great-circle distance from the epicenter location (-20.5°N, -175.4°E) as identified by the US Geological Survey for the eruption induced magnitude M 5.8 earthquake origin (USGS, 2022). Figure 1 provides relevant geometry information and great-circle distance contours from the eruption location, as well as a great circle oriented at 26 and 206° azimuth from the epicenter. Superimposed is a background global map of GNSS TEC measurements at three post-eruption instances. Great circles assume 300 km height, characteristic of approximate ionospheric F region altitudes near the peak of the plasma population. The maximum great-circle distance is located at (4.6°E, 20.4°N) near Sahara in North Africa. New Zealand was 2-4,000 km away, central US 12,000 km, South Africa 14,000 km, and Europe 18,000 km. Upper atmospheric perturbations beyond 10,000 km have never been able to be examined before this eruption.

Both northern ($|\mathrm{Azimuth}| < 90°$) and southern (($|\mathrm{Azimuth}| > 90°$) great circles pass high latitudes. The great circle is presumed to be the shortest path along which disturbance energy and momentum in the neutral gas will flow radially from the epicenter. We note that, although global TEC is not evenly sampled by ground receivers with large gaps over the oceans, each observation is useful in distance-time analysis. Thus, in contrast to typical TEC studies, the distribution of disturbance propagation observations do not suffer severe gaps as demonstrated in the following distance-time figures. Themens et al. (2022) also presented these type of distance-time figures, and our analysis is similar except that we provide propagation estimates also based on azimuth bearing of great circles. The approach allows us to precisely locate propagation signatures and clearly identify inbound waves.

The distance-time variation of dTEC illustrated in Figure 2 indicate dramatic development of disturbance global propagation over a prolonged period. The southward propagation from Tonga to Africa sectors via the southern high-latitude region shows a defined envelope, as marked by fiducial arrows bounding enhanced disturbance (in dTEC) as a function of distance and UT. The width of the envelopes is ~ 8 hours in time with $\sim$350 m/s slopes. Results show that dTEC fluctuations reached the furthest distance at $\sim$20,000 km via the southern polar region. Northward propagation is predominately similar as indicated by envelope lines and their slopes, and also reached $\sim$20,000 km distance where it encountered the southern outbound propagation. Although dTEC signals became weak at several distances of 14,000 km and 16,000 km, corresponding to European sectors and midlatitudes, propagation signals reappeared beyond those distances perhaps due to wave modulation. In the following discussion, we examine detailed regional characteristics in near-field and far-field regions and provide further evidence of ionospheric perturbation arrivals.

3.2 Near-field ionospheric disturbances

GNSS TEC measurements indicate immediate and vast near-field Tonga event atmospheric perturbations as demonstrated in Themens et al. (2022) and Figure 3. The earliest response was a clear positive dTEC occurring within 200 km of the epicenter almost instantaneously following the eruption at ∼04:15UT. This response, with ∼1 km/s radial propagation for the first 20 min, was an indication of supersonic infrasonic waves typically seen (as Rayleigh waves) during earthquake events (see Astafyeva, 2019, and references therein). Immediately following, two enormous shocks occurred with dTEC magnitudes up to 3 TECu (1TECu = 10^{16} electrons/m^2). Radial propagation initially occurred at ∼700 m/s speed, gradually slowing down to ∼450 m/s, and reached ∼5,000 km distance. The initial waves were clearly identifiable over the northern New Zealand area (∼1,500 km away from the epicenter) as early as ∼ 0500 UT (e.g., Figure 3) and, specifically, at ∼06:20 UT with 2-D fronts (Figure 1b). Subsequent waves were characterized by smaller amplitudes (0.1–0.2 TECu) at lower and relatively stable speeds of ∼360 m/s. These amplitudes were well within typical amplitudes for medium to large scale TIDs. These fluctuations had ∼10-30 min quasi-periodicity for at least 8 hours (see Figures 3a,b,c, and also Figure 2). The 2-D wave fronts exhibited horizontal wavelengths initially 500-1000 km (Figure 1b) and later ∼300 km (Figure 1c).

3.3 Far-field ionospheric responses

Beyond the near-field, outbound ionospheric responses propagated into different regions of the world. Within 195-315° azimuth bearing of the great circles, the disturbance propagation signals were evident between 13-18,000 km (Figure 4a), particularly over South Africa, with large amplitudes and consistent ∼ 350 m/s propagation speeds. These disturbances lasted for at least 5 hours with up to ∼10-30 min periods, arriving via southern great circles (Figure 1a). These results were derived as dTEC averages in time and distance with 1 minute bins size in time and 10 km bin size in distance. 2-D wavefronts during the shock arrival showed well organized disturbances with 500-1000 km wavelengths (Figure 4c), similar to Figure 1b in the near-field.

The continental US (CONUS) has dense receiver networks, therefore only a narrow range of azimuths (55-58°) are taken into account, to minimize decoherence of the wave signature due to regional deviations in the group velocity of the wave fronts. Such deviations can be caused by e.g., prevailing wind velocity, atmospheric pressure, propagation direction (Taylor, 1932), and the ionospheric conditions. Figure 4b shows the first sign of disturbance arrival in the west coast (8-9,000 km distance) at ∼11-12:00 UT, and the earliest front departed off the east coast at 13,000 km by ∼16:00 UT. Throughout, propagation speed remained at ∼350 m/s. Some samples of 2-D wavefronts are shown in Figure 4e. dTEC enhancements were aligned with iso-distance lines, and separated zonally by ∼500 km spacing (wavelengths).

Simultaneously, background TIDs were present, likely associated with geomagnetic disturbances during the recovery from a geospace storm with minimum Dst -94 nT at 23:00 UT on 2022-01-14 (according to WDC Kyoto, 2022b). The substorm activity measured by the AE index (WDC Kyoto, 2022a) indicated an onset after 1100 UT and multiple hourly enhancements reaching ∼500 nT throughout the rest of the UT day. Thus the ionospheric short-term disturbance was characterized by hourly enhancements of TID amplitudes almost simultaneously in latitude and longitude over CONUS, well correlated to AE activity. Post-sunrise TIDs were evident in the US east coast, propagating eastward at ∼300 m/s with 20-30 min periods, similar to what were reported in Zhang et al. (2021). Background TIDs include also gravity waves in certain region potentially linked to the strong stratospheric polar vortex (Sato and Yoshiki, 2008; Becker and Vadas, 2018; Bossert et al., 2020). These background TIDs occurred on the distance-time plot as simultaneous enhancement bands, slant bands, and possibly other features. The arriving eruption-induced fluctuations segmented these pre-existing TIDs fronts into smaller structures elongated along iso-distance lines, and had sharply different characteristics that can be distinguished in the distance-time plot (Figure 4b).

3.4 Wave propagation return to Tonga

Ionospheric fluctuations continued to propagate through the eruption antipode in North Africa toward Tonga on the next day. These returning TIDs were most evident over South Africa (Figure 4q) where the disturbance phase was clearly toward shorter distance (light-blue arrows), starting at 03:00 UT at 15,000 km distance. The speed was ∼350 m/s. Figure 4e shows an example of wavefronts associated with the returning TIDs at 03:30 UT on 2022-01-16, close to local sunrise time. The timing of the returning TIDs is approximately consistent with propagation from the most distant point to South Africa along the great-circle Tonga – CONUS – Europe – South Africa – Tonga path (Figure 1a). Returning TIDs occurred also across the CONUS over a prolonged period for ∼ 8 hours initially at ∼0600 UT at 13,000 km (the US east coast) (see light-blue arrows in Figure 4b), following a longer path of Tonga – southern high latitudes – South Africa – Europe – CONUS.

In the near field, clear indications occurred of the wave returning to New Zealand (Figure 3c) at 2,500-3,000 km distance from Tonga by ∼13:00 UT on 16 January (or to Tonga by ∼15:00 UT on 16 January), after traveling nearly 1.5 days along the complete great-circle. This timing is roughly consistent with a propagation at ∼350 m/s speed around the full great-circle.

3.5 Discussion

During the TID global propagation, the horizontal phase speed varied between 300-350 m/s depending on propagation direction. For example, Figure 2 marks a southward propagation (red arrow) at 300 m/s. However, these speed estimations are generally consistent with infrasonic detection of pressure wave arrival at individual stations around the world, e.g., in northern Europe (Norstar Website, 2022) using the network established to monitor compliance with the Comprehensive Nuclear Test Ban Treaty and over CONUS using the pressure altimeter observations (Iowa Environmental Mesonet, 2022). Lamb waves travel at the sound speed, typically 300-350 m/s in the troposphere, and can exist at any period. Although their energy is confined to the troposphere, their amplitudes increase exponentially with height due to decreasing density. Their wave energy can leak into the upper atmosphere when Lamb waves with ∼300 m/s horizontal phase speed are resonant with the atmosphere, as can be the case with acoustic and gravity waves (Bretherton, 1969; Lindzen and Blake, 1972; Nishida et al., 2014). Lamb waves with ∼319 m/s phase speed were previously identified as an atmospheric wave response to the Krakatoa eruption (Symons, 1888; Taylor, 1932). Similar Lamb waves were also detected by very sensitive microbarographs during the St. Helens eruption (Mikumo and Bolt, 1985) and the Sumatra-Andaman earthquake (Mikumo et al., 2008).

A significant portion of our GNSS observations occurred inland, where direct tsunami wave contribution to these TID results may be ignored. Furthermore, an additional argument against the presumption of tsunami wave presence with 10-30 min periodicity and 300-350 m/s travel speed as noted earlier: tsunami waves were reported to occur in the US west coast at 15:30-16:00 UT (NOAA DART and NOAA/NOS/CO-OPS Data, 2022) consistent with an anticipated 210-220 m/s propagation speed across the Pacific ocean. This is clearly different from observed ionospheric wave propagation which arrived at least ∼4 hours earlier than the tsunami waves in the US west coast. Nevertheless, continued community study is recommended to further clarify the roles of tsunami and gravity wave interactions and the factors that are potentially responsible for their different propagation speeds (Makela et al., 2011; Kherani et al., 2016; Bagiya et al., 2017).

The earliest wavefronts could be seen traveling around the globe three times, passing six times over the CONUS over 100 hrs since the eruption (Figures 4b,f); the pass 6 over CONUS occurred at $\sim$05:00 UT on 2022-01-19 at 13,000 km (but is not shown here due to the space limit). The travel time around the globe in the direction of Earth's rotation (eastward) was 34.8 ± 0.7 hours and in the opposite direction 36.0 ± 0.7 hours. The error standard deviations are roughly one order of magnitude estimates based on visual inspection.The measured propagation speed and the number of observed passes of the atmospheric wave are comparable to those reported with the Krakatoa eruption (Symons, 1888). Time periods before and after the eruption were processed with the same analysis, and no similar traces corresponding to ones shown in Figures 4b,f were observed before the eruption.

4 SUMMARY

The 2021 Tonga volcano eruption caused enormous and truly global perturbations in the ionosphere and thermosphere over an extended period. Ionospheric disturbances were observed traveling three times around the globe. They returned back to Tonga every 1.5 days. The ionospheric responses were characterized by an immediate supersonic ($\sim$1 km/s) plasma density impulse, and two shock waves with substantial amplitudes (3 TECu) and 600-700 m/s horizontal speeds in $\leq$5,000 km near-field regions including New Zealand to the south, and Hawaii to the north. Subsequently, persistent (lasting 8 hours) slower-propagating TIDs developed with 10-30 min periods, most significantly in the near-field ($<$5,000 km radius). Far-field wave effects include also 10-30 min periodical oscillations lasting for a few hours, but more significantly, TID shock fronts were clearly organized based on the distance from Tonga in the continental US ($\sim$12,000 km distances) and midlatitude west Europe ($\sim$18,000 km distances), with the two destination regions connected via the northern high-latitude region along the great circle with an origin in Tonga. A similar path of global wave propagation occurred in the southern hemisphere along a New Zealand - southern polar region - South Africa route. These far-field globally propagating waves had 500-1000 km horizontal wavelengths.

These disturbances resulted from eruption-induced perturbations at frequencies of acoustic waves (including Lamb waves) and gravity waves. Eruption-associated tsunami waves were slower than the main component of ionospheric waves that propagated globally and are therefore unlikely responsible for the TID global propagation. The presumption of Lamb wave global propagation at 300-350 m/s is consistent with our main observational results. These waves provide one of the main carriers for eruption energy leaking into the upper atmosphere because of atmospheric resonance to forcing provided by these waves at $\sim$300 m/s phase speed, equivalent to the speed of sound in the troposphere. These ionospheric propagation results are also consistent with data from infrasonic global detections and other pressure wave detections. Our multi-sensor investigation, based on 5000+ world-wide GNSS receivers, reveals the unprecedented depth, severity, and extent of disturbances in the whole atmosphere in vertical and horizontal dimensions that occur during an extremely devastating geohazard impact. This is yet another demonstration of the ionosphere acting as a sensitive detector for atmospheric waves.

CONFLICT OF INTEREST STATEMENT

The authors declare that the research was conducted in the absence of any commercial or financial relationships that could be construed as a potential conflict of interest.

AUTHOR CONTRIBUTIONS

SRZ was responsible for differential TEC derivation, science analysis of the observational results, preparing the initial manuscript and organizing team efforts. JV contributed initial figures for comparisons, science analysis, discussion, and organizing team research. EA was responsible for Beidou GNSS data processing. LPG conducted analysis of TIDs that could potentially be linked to meteorological disturbances. PJE contributed substantially to the manuscript development. AJC was responsible for GNSS data management. WR was responsible for software development of GNSS data processing and daily GNSS data processing. AS contributed examining satellite data. All members contributed to science discussion and manuscript development.

FUNDING

GNSS TEC data products and access through the Madrigal distributed data system are provided to the community by the Massachusetts Institute of Technology under support from US National Science Foundation grant AGS-1952737. MIT staff members were partially supported by NASA grants 80NSSC21K1775, 80NSSC21K1310, 80NSSC22K0171, and 80NSSC19K0834, AFOSR MURI grant FA9559-16-1-0364, NSF grant AGS-2033787 and ONR grant N00014-17-1-2186.

ACKNOWLEDGMENTS

Data for TEC processing is provided from the following organizations: UNAVCO, Scripps Orbit and Permanent Array Center, Institut Geographique National, France, International GNSS Service, The Crustal Dynamics Data Information System (CDDIS), National Geodetic Survey, Instituto Brasileiro de Geografia e Estatística, RAMSAC CORS of Instituto Geográfico Nacional de la República Argentina, Arecibo Observatory, Low-Latitude Ionospheric Sensor Network (LISN), Topcon Positioning Systems, Inc., Canadian High Arctic Ionospheric Network, Institute of Geology and Geophysics, Chinese Academy of Sciences, China Meteorology Administration, Centro di Ricerche Sismologiche, Système d'Observation du Niveau des Eaux Littorales (SONEL), RENAG : REseau NAtional GPS permanent, GeoNet - the official source of geological hazard information for New Zealand, GNSS Reference Networks, Finnish Meteorological Institute, and SWEPOS - Sweden.

DATA AVAILABILITY STATEMENT

GNSS TEC data products and access through the Madrigal distributed data system [http://openmadrigal.org] are provided to the community by the Massachusetts Institute of Technology. The datasets generated for this study can be found here: [http://aeronomy.haystack.mit.edu/muri/share/tonga/].

REFERENCES

Aa, E., Zhang, S.-R., Erickson, P. J., Coster, A. J., Goncharenko, L. P., Varney, R. H., et al. (2021). Salient Midlatitude Ionosphere-Thermosphere Disturbances Associated With SAPS During a Minor but

Geo-Effective Storm at Deep Solar Minimum. *Journal of Geophysical Research: Space Physics* 126, e2021JA029509

Artru, J., Ducic, V., Kanamori, H., Lognonné, P., and Murakami, M. (2005). Ionospheric detection of gravity waves induced by tsunamis. *Geophysical Journal International* 160, 840–848. doi:10.1111/j.1365-246X.2005.02552.x

Astafyeva, E. (2019). Ionospheric Detection of Natural Hazards. *Reviews of Geophysics* 3, 673

Astafyeva, E. I. and Afraimovich, E. L. (2006). Long-distance traveling ionospheric disturbances caused by the great Sumatra-Andaman earthquake on 26 December 2004. *Earth, Planets and Space* 58, 1025–1031

Azeem, I., Vadas, S. L., Crowley, G., and Makela, J. J. (2017). Traveling ionospheric disturbances over the United States induced by gravity waves from the 2011 Tohoku tsunami and comparison with gravity wave dissipative theory. *Journal of Geophysical Research: Space Physics* 122, 3430–3447

Bagiya, M. S., Kherani, E., Sunil, P., Sunil, A., Sunda, S., and Ramesh, D. (2017). Origin of the ahead of tsunami traveling ionospheric disturbances during Sumatra tsunami and offshore forecasting. *Journal of Geophysical Research: Space Physics* 122, 7742–7749

Becker, E. and Vadas, S. L. (2018). Secondary gravity waves in the winter mesosphere: Results from a high-resolution global circulation model. *Journal of Geophysical Research: Atmospheres* 123, 2605–2627

Bossert, K., Vadas, S. L., Hoffmann, L., Becker, E., Harvey, V. L., and Bramberger, M. (2020). Observations of stratospheric gravity waves over europe on 12 january 2016: The role of the polar night jet. *Journal of Geophysical Research: Atmospheres* 125, e2020JD032893

Bretherton, F. (1969). Lamb waves in a nearly isothermal atmosphere. *Quarterly Journal of the Royal Meteorological Society* 95, 754–757

Chou, M.-Y., Lin, C. C. H., Shen, M.-H., Yue, J., Huba, J. D., and Chen, C.-H. (2018). Ionospheric disturbances triggered by SpaceX Falcon Heavy. *Geophysical Research Letters* 45, 6334–6342. doi:10.1029/2018GL078088

Chum, J., Liu, J. Y., Podolská, K., and Šindelářová, T. (2018). Infrasound in the ionosphere from earthquakes and typhoons. *Journal of Atmospheric and Solar-Terrestrial Physics* 171, 72–82

Coster, A., Herne, D., Erickson, P., and Oberoi, D. (2012). Using the Murchison Widefield Array to observe midlatitude space weather. *Radio Science* 47, RS0K07. doi:10.1029/2012RS004993

Crowley, G., Azeem, I., Reynolds, A., Duly, T. M., McBride, P., Winkler, C., et al. (2016). Analysis of traveling ionospheric disturbances (TIDs) in GPS TEC launched by the 2011 Tohoku earthquake. *Radio Science* 51, 507–514

Dautermann, T., Calais, E., and Mattioli, G. S. (2009). Global positioning system detection and energy estimation of the ionospheric wave caused by the 13 july 2003 explosion of the soufrière hills volcano, montserrat. *Journal of Geophysical Research: Solid Earth* 114. doi:https://doi.org/10.1029/2008JB005722

Ding, F., Wan, W., Ning, B., and Wang, M. (2007). Large-scale traveling ionospheric disturbances observed by GPS total electron content during the magnetic storm of 29-30 October 2003. *Journal of Geophysical Research (Space Physics)* 112, A06309. doi:10.1029/2006JA012013

Duncombe, J. (2022). The surprising reach of Tonga's giant atmospheric waves. *Eos: AGU Science News* 103

England, S. L., Greer, K. R., Zhang, S.-R., Evans, S., Solomon, S. C., Eastes, R. W., et al. (2021). First comparison of travelling atmospheric disturbances observed in the middle thermosphere by GOLD to travelling ionospheric disturbances seen in ground-based total electron content observations. *Journal of Geophysical Research: Space Physics* , e2021JA029248

Galvan, D. A., Komjathy, A., Hickey, M. P., Stephens, P., Snively, J., Song, Y. T., et al. (2012). Ionospheric signatures of Tohoku-Oki tsunami of March 11, 2011: Model comparisons near the epicenter. *Radio Science* 47, 1–10

[Dataset] Garvin, J. (2022). Dramatic Changes at Hunga Tonga-Hunga Ha'apai. https://earthobservatory.nasa.gov/images/149367/dramatic-changes-at-hunga-tonga-hunga-haapai. [Online; accessed 3-Feb 2022]

Hao, Y., Xiao, Z., and Zhang, D. (2012). Multi-instrument observation on co-seismic ionospheric effects after great Tohoku earthquake. *Journal of Geophysical Research: Space Physics* 117

Hao, Y.-Q., Xiao, Z., and Zhang, D.-H. (2006). Responses of the Ionosphere to the Great Sumatra Earthquake and Volcanic Eruption of Pinatubo. *Chinese Physics Letters* 23, 1955

Heki, K. (2006). Explosion energy of the 2004 eruption of the asama volcano, central japan, inferred from ionospheric disturbances. *Geophysical Research Letters* 33. doi:https://doi.org/10.1029/2006GL026249

Heki, K. and Ping, J. (2005). Directivity and apparent velocity of the coseismic ionospheric disturbances observed with a dense GPS array. *Earth and Planetary Science Letters* 236, 845–855

[Dataset] Iowa Environmental Mesonet (2022). Pressure altimeter data movies: Past IEM Features tagged: Tonga. https://mesonet.agron.iastate.edu/onsite/features/tags/tonga.html. [Online; accessed 3-Feb-2022]

Kherani, E., Rolland, L., Lognonné, P., Sladen, A., Klausner, V., and de Paula, E. (2016). Traveling ionospheric disturbances propagating ahead of the Tohoku-Oki tsunami: a case study. *Geophysical Journal International* 204, 1148–1158

Kieffer, S. W. (1981). Blast dynamics at mount St Helens on 18 May 1980. *Nature* 291, 568–570

Komjathy, A., Yang, Y.-M., Meng, X., Verkhoglyadova, O., Mannucci, A. J., and Langley, R. B. (2016). Review and perspectives: Understanding natural-hazards-generated ionospheric perturbations using gps measurements and coupled modeling. *Radio Science* 51, 951–961

Lindzen, R. S. and Blake, D. (1972). Lamb waves in the presence of realistic distributions of temperature and dissipation. *Journal of Geophysical Research: Space Physics (1978–2012)* 77, 2166–2176

Liu, C. H., Klostermeyer, J., Yeh, K. C., Jones, T. B., Robinson, T., Holt, O., et al. (1982). Global dynamic responses of the atmosphere to the eruption of Mount St. Helens on May 18, 1980. *Journal of Geophysical Research: Space Physics (1978–2012)* 87, 6281–6290

Liu, J., Tsai, H., Lin, C., Kamogawa, M., Chen, Y., Lin, C., et al. (2010). Coseismic ionospheric disturbances triggered by the Chi-Chi earthquake. *Journal of Geophysical Research: Space Physics* 115

Liu, J., Tsai, Y., Chen, S., Lee, C., Chen, Y., Yen, H., et al. (2006). Giant ionospheric disturbances excited by the M9.3 Sumatra earthquake of 26 December 2004. *Geophysical Research Letters* 33

Lyons, L. R., Nishimura, Y., Zhang, S.-R., Coster, A. J., Bhatt, A., Kendall, E., et al. (2019). Identification of auroral zone activity driving large-scale traveling ionospheric disturbances. *Journal of Geophysical Research: Space Physics*

Makela, J., Lognonné, P., Hébert, H., Gehrels, T., Rolland, L., Allgeyer, S., et al. (2011). Imaging and modeling the ionospheric airglow response over Hawaii to the tsunami generated by the Tohoku earthquake of 11 March 2011. *Geophysical Research Letters* 38

Mikumo, T. and Bolt, B. A. (1985). Excitation mechanism of atmospheric pressure waves from the 1980 Mount St Helens eruption. *Geophysical Journal International* 81, 445–461

Mikumo, T., Shibutani, T., Le Pichon, A., Garces, M., Fee, D., Tsuyuki, T., et al. (2008). Low-frequency acoustic-gravity waves from coseismic vertical deformation associated with the 2004 Sumatra-Andaman earthquake (Mw=9.2). *Journal of Geophysical Research: Solid Earth* 113

Newhall, C. G. and Self, S. (1982). The volcanic explosivity index (vei) an estimate of explosive magnitude for historical volcanism. *Journal of Geophysical Research: Oceans* 87, 1231–1238

Nishida, K., Kobayashi, N., and Fukao, Y. (2014). Background Lamb waves in the Earth's atmosphere. *Geophysical Journal International* 196, 312–316

[Dataset] NOAA DART and NOAA/NOS/CO-OPS Data (2022). January 15, 2022 Tonga Tsunami. `https://www.ngdc.noaa.gov/hazard/dart/2022tonga.html`. [Online; accessed 3-Feb-2022]

[Dataset] Norstar Website (2022). Enorm trykkbølge registrert etter vulkaneksplosjonen på Tonga. `https://www.norsar.no/i-fokus/enorm-trykkbolge-registrert-etter-vulkaneksplosjonen-pa-tonga`. [Online; accessed 3-Feb-2022]

Rideout, W. and Coster, A. (2006). Automated GPS processing for global total electron content data. *GPS Solutions* 10, 219–228

Roberts, D. H., Klobuchar, J. A., Fougere, P. F., and Hendrickson, D. H. (1982). A large-amplitude traveling ionospheric disturbance produced by the May 18, 1980, explosion of Mount St. Helens. *Journal of Geophysical Research: Space Physics (1978–2012)* 87, 6291–6301

Saito, A., Fukao, S., and Miyazaki, S. (1998). High resolution mapping of TEC perturbations with the GSI GPS Network over Japan. *Geophysical Research Letters* 25, 3079–3082. doi:10.1029/98GL52361

Sato, K. and Yoshiki, M. (2008). Gravity wave generation around the polar vortex in the stratosphere revealed by 3-hourly radiosonde observations at syowa station. *Journal of the Atmospheric Sciences* 65, 3719–3735

Savitzky, A. and Golay, M. J. E. (1964). Smoothing and differentiation of data by simplified least squares procedures. *Analytical Chemistry* 36, 1627–1639

Sheng, C., Deng, Y., Zhang, S.-R., Nishimura, Y., and Lyons, L. R. (2020). Relative Contributions of Ion Convection and Particle Precipitation to Exciting Large-Scale Traveling Atmospheric and Ionospheric Disturbances. *Journal of Geophysical Research: Space Physics* 125, 1667

Symons, G. J. (1888). *The Eruption of Krakatoa, and Subsequent Phenomena: Report of the Krakatoa Committee of the Royal Society* (Wiley Online Library)

Taylor, G. I. (1932). The resonance theory of semidiurnal atmospheric oscillations. *Roy. Meteorol. Soc.* 4[9], 41–52

Themens, D. R., Watson, C., Žagar, N., Vasylkevych, S., Elvidge, S., Mccaffrey, A., et al. (2022). Global propagation of ionospheric disturbances associated with the 2022 Tonga Volcanic Eruption. *Earth and Space Science Open Archive* , 25doi:10.1002/essoar.10510350.1

Tsugawa, T., Otsuka, Y., Coster, A. J., and Saito, A. (2007). Medium-scale traveling ionospheric disturbances detected with dense and wide TEC maps over North America. *Geophysical Research Letters* 34, L22101. doi:10.1029/2007GL031663

[Dataset] USGS (2022). M 5.8 Volcanic Eruption - 68 km NNW of Nuku'alofa, Tonga. `https://earthquake.usgs.gov/earthquakes/eventpage/us7000gc8r/origin/detail`. [Online; accessed 3-Feb-2022]

Vierinen, J., Coster, A. J., Rideout, W. C., Erickson, P. J., and Norberg, J. (2016). Statistical framework for estimating GNSS bias. *Atmospheric Measurement Techniques* 9, 1303–1312. doi:10.5194/amt-9-1303-2016

[Dataset] WDC Kyoto (2022a). World Data Center for Geomagnetism, Kyoto: Real-time AE index. `http://wdc.kugi.kyoto-u.ac.jp/ae_realtime/202201/index_20220115.html`. [Online; accessed 3-Feb-2022]

[Dataset] WDC Kyoto (2022b). World Data Center for Geomagnetism, Kyoto: Real-time Dst Index. `http://wdc.kugi.kyoto-u.ac.jp/dst_realtime/202201/index.html`. [Online; accessed 3-Feb-2022]

Zakharenkova, I., Astafyeva, E., and Cherniak, I. (2016). Gps and glonass observations of large-scale traveling ionospheric disturbances during the 2015 st. patrick's day storm. *Journal of Geophysical Research: Space Physics* 121, 12–138

Zettergren, M. D. and Snively, J. B. (2015). Ionospheric response to infrasonic-acoustic waves generated by natural hazard events. *Journal of Geophysical Research: Space Physics* 120, 8002–8024

Zhang, S.-R., Coster, A. J., Erickson, P. J., Goncharenko, L. P., Rideout, W., and Vierinen, J. (2019a). Traveling Ionospheric Disturbances and Ionospheric Perturbations Associated With Solar Flares in September 2017. *Journal of Geophysical Research: Space Physics* 60, 895

Zhang, S.-R., Erickson, P. J., Coster, A. J., Rideout, W., Vierinen, J., Jonah, O., et al. (2019b). Subauroral and polar traveling ionospheric disturbances during the 7-9 September 2017 storms. *Space Weather* , 2019SW002325

Zhang, S.-R., Erickson, P. J., Gasque, L. C., Aa, E., Rideout, W., Vierinen, J., et al. (2021). Electrified Postsunrise Ionospheric Perturbations at Millstone Hill. *Geophyical Research Letters* 48, e2021GL095151

Zhang, S.-R., Erickson, P. J., Goncharenko, L. P., Coster, A. J., Rideout, W., and Vierinen, J. (2017). Ionospheric bow waves and perturbations induced by the 21 August 2017 solar eclipse. *Geophyical Research Letters* 44, 12,067–12,073

Zhao, B. and Hao, Y. (2015). Ionospheric and geomagnetic disturbances caused by the 2008 wenchuan earthquake: A revisit. *Journal of Geophysical Research: Space Physics* 120, 5758–5777

FIGURE CAPTIONS

Figure 1 Geometry information of Tonga eruption impact distance (green lines) determined based on the great circle at 300 km height (white or yellow lines) that connect to the eruption region. Iso-distance lines up to 20,000 km are separated at 2,000 km interval. Great circles start at the Tonga epicenter for azimuth 26/206°. Background colors are differential TEC measured from ground-based receivers to GPS, GLONASS and Beidou navigation systems for the early stage of upper atmospheric responses at 0830 UT (a), 0620 UT (b), and 0920 UT (c). TID wave fronts are annotated by red and blue arrows in the three maps.Cyan lines are iso-geomagnetic latitudes at the 15° interval.

Figure 2 Distance-UT variation of dTEC for disturbance propagation southward (negative distance) and northward (positive distance) along the great circle paths at 300 km altitude on 15 January. White arrows provide envelope lines encompassing the ionospheric disturbances. The slopes of these lines are $\sim$350 m/s. Dashed lines with larger slopes ($\sim$700m/s) follow the initial ionospheric shocks which terminated after 5,000-6,000 km. Red arrows marks the radial propagation in the European sector which is zoomed out in Figure 4b.

Figure 3 Near-field observations of initial and subsequent GNSS TEC fluctuations: the distance-time (regardless direction) variation within 5,000 km 6 hours following the eruption (a); regional GNSS TEC fluctuations in New Zealand showing the evolution of fluctuation periodicities in space and time (b); near-field TIDs, the same as (a) but over 48 hours (c) with red arrows marking the outbound $\sim$350 m/s wave propagation, and black arrows marking the potential returning waves at $\sim$350 m/s into Tonga after 15:00 UT on the following day 16 January. See Figure 4 for further indications of returning waves.

Figure 4 Far-field ionospheric disturbances in selected regions: distance-time variation over Europe-Africa sectors with 195-315°azimuth bearing (a) and the continental US (CONUS) with 55-58°azimuth bearing (b) over 48 hours between 2022-01-15$\sim$16. Green solid lines and arrows mark the radial propagation for outbound waves, at $\sim$350 m/s (slope); light-blue lines and arrows show the inbound waves toward Tonga on 2022-01-16. (c-d) show TID wavefronts over South Africa corresponding to (a) at 17:00 UT (outbound) and 03:30 UT (inbound). (e) shows TID wavefronts at 13:38 UT over CONUS corresponding to (b), Arrows in (c-e) indicate the radial outbound and inbound propagation along the great circles (marked by white dotted lines). (f) Same as (b) but for 2022-01-17$\sim$18.

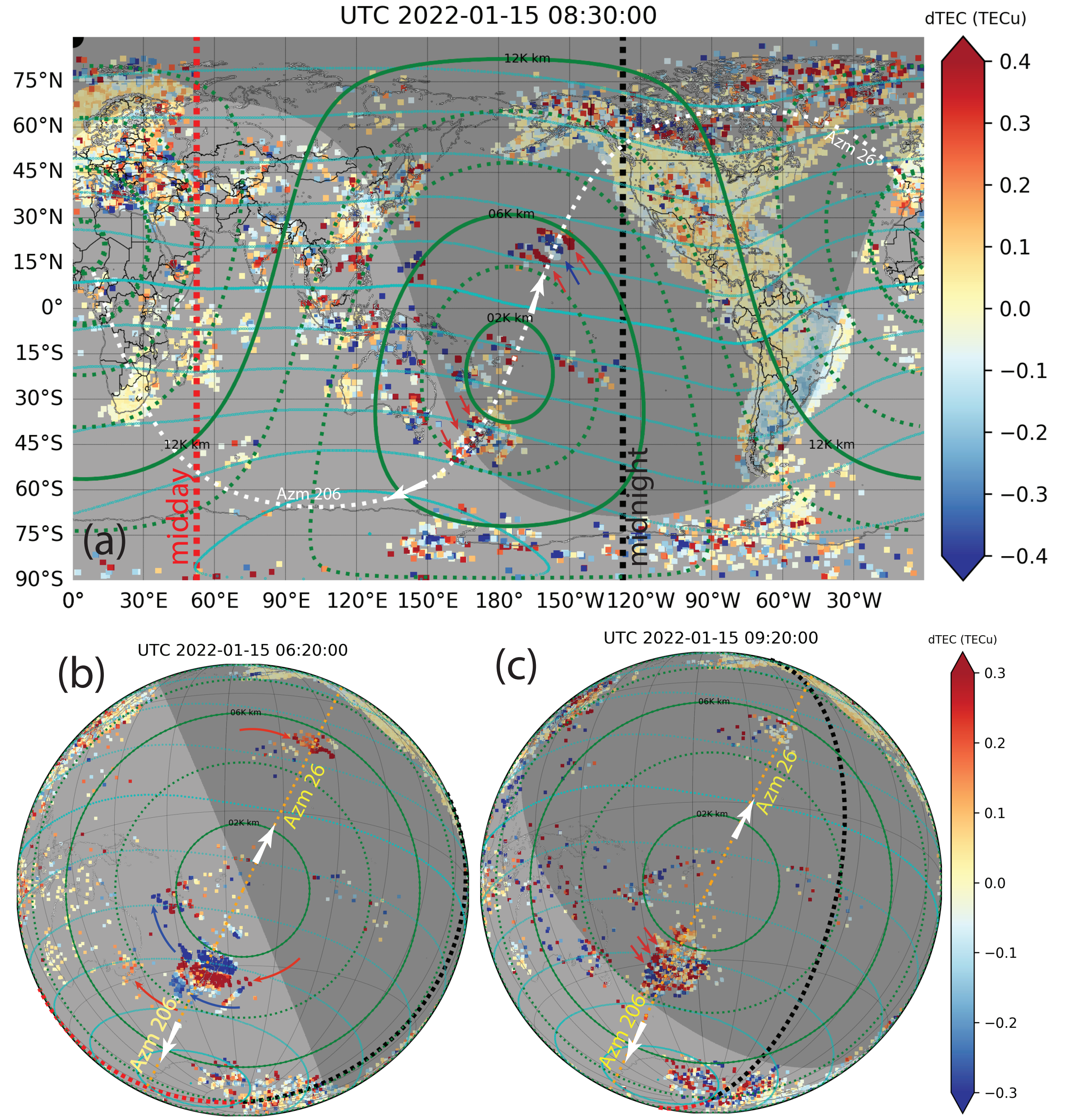

Figure 1. Geometry information of Tonga eruption impact distance (green lines) determined based on the great circle at 300 km height (white or yellow lines) that connect to the eruption region. Iso-distance lines up to 20,000 km are separated at 2,000 km interval. Great circles start at the Tonga epicenter for azimuth 26/206°. Background colors are differential TEC measured from ground-based receivers to GPS, GLONASS and Beidou navigation systems for the early stage of upper atmospheric responses at 0830 UT (a), 0620 UT (b), and 0920 UT (c). TID wave fronts are annotated by red and blue arrows in the three maps. Cyan lines are iso-geomagnetic latitudes at the 15° interval.

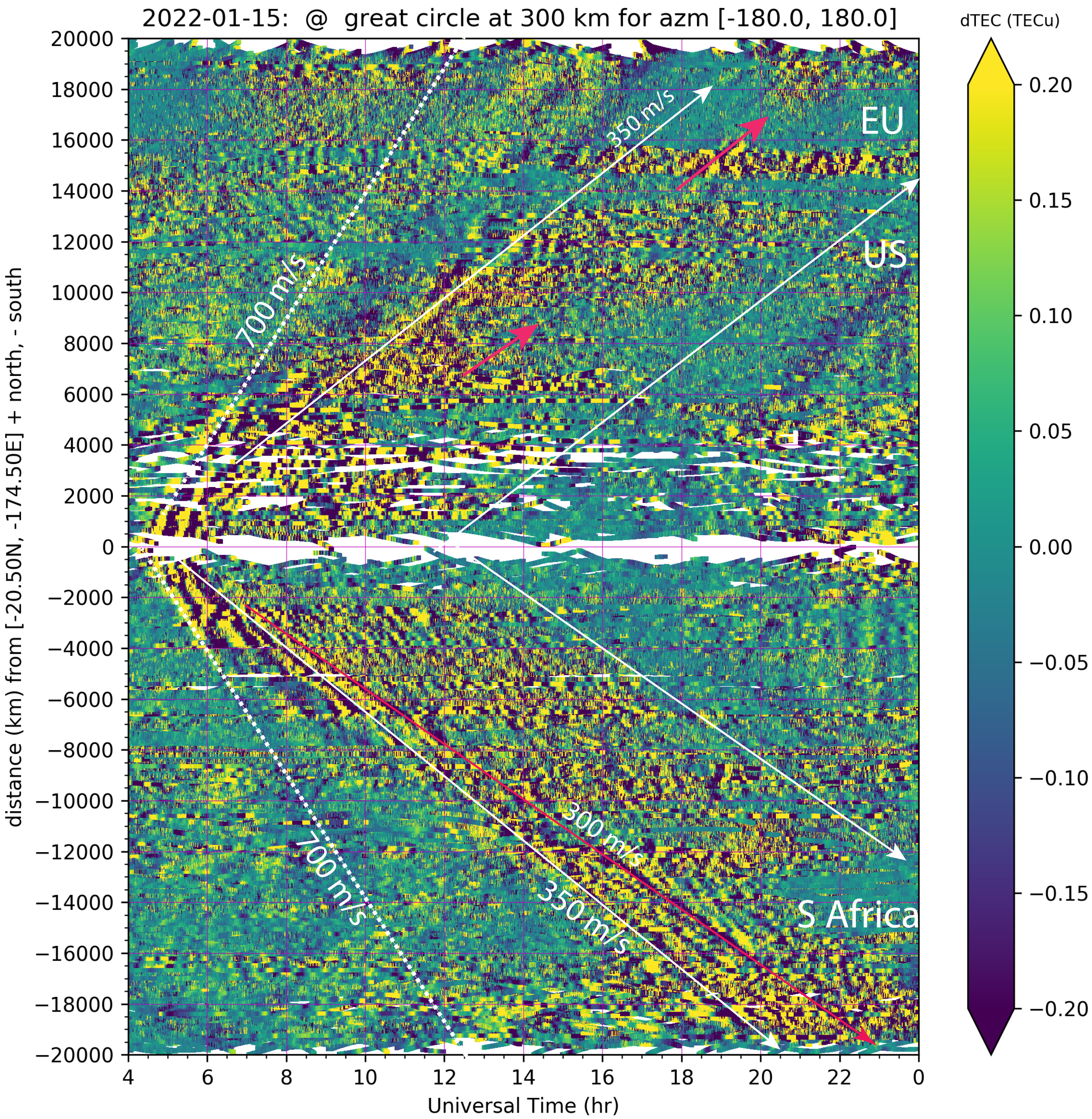

Figure 2. Distance-UT variation of dTEC for disturbance propagation southward (negative distance) and northward (positive distance) along the great circle paths at 300 km altitude on 15 January. White arrows provide envelope lines encompassing the ionospheric disturbances. The slopes of these lines are ∼350 m/s. Dashed lines with larger slopes (∼700m/s) follow the initial ionospheric shocks which terminated after 5,000-6,000 km. Red arrows marks the radial propagation in the European sector which is zoomed out in Figure 4b.

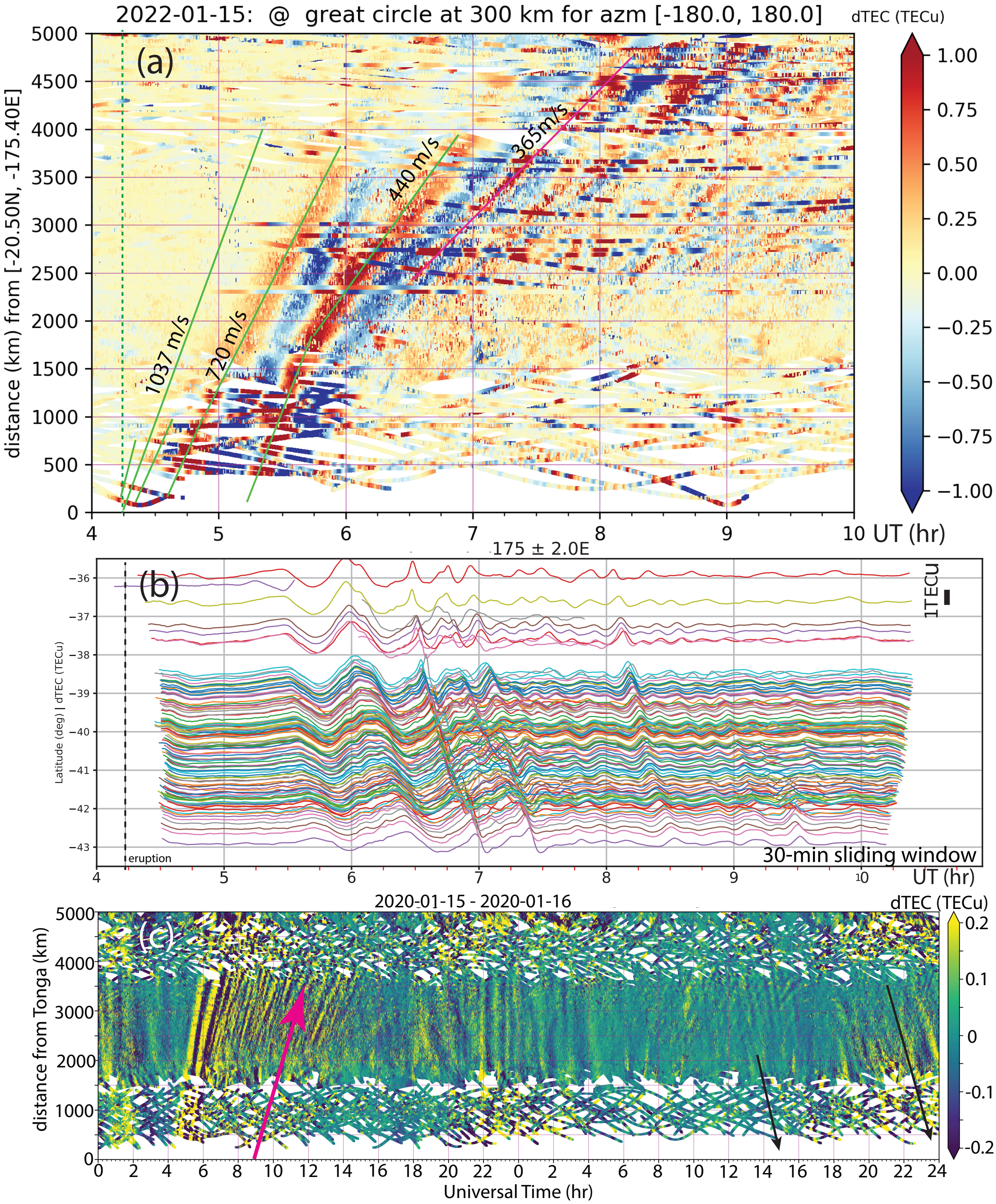

Figure 3. Near-field observations of initial and subsequent GNSS TEC fluctuations: the distance-time (regardless direction) variation within 5,000 km 6 hours following the eruption (a); regional GNSS TEC fluctuations in New Zealand showing the evolution of fluctuation periodicities in space and time (b); near-field TIDs, the same as (a) but over 48 hours (c) with red arrows marking the outbound ∼350 m/s wave propagation, and black arrows marking the potential returning waves at ∼350 m/s into Tonga after 15:00 UT on the following day 16 January. See Figure 4 for further indications of returning waves.

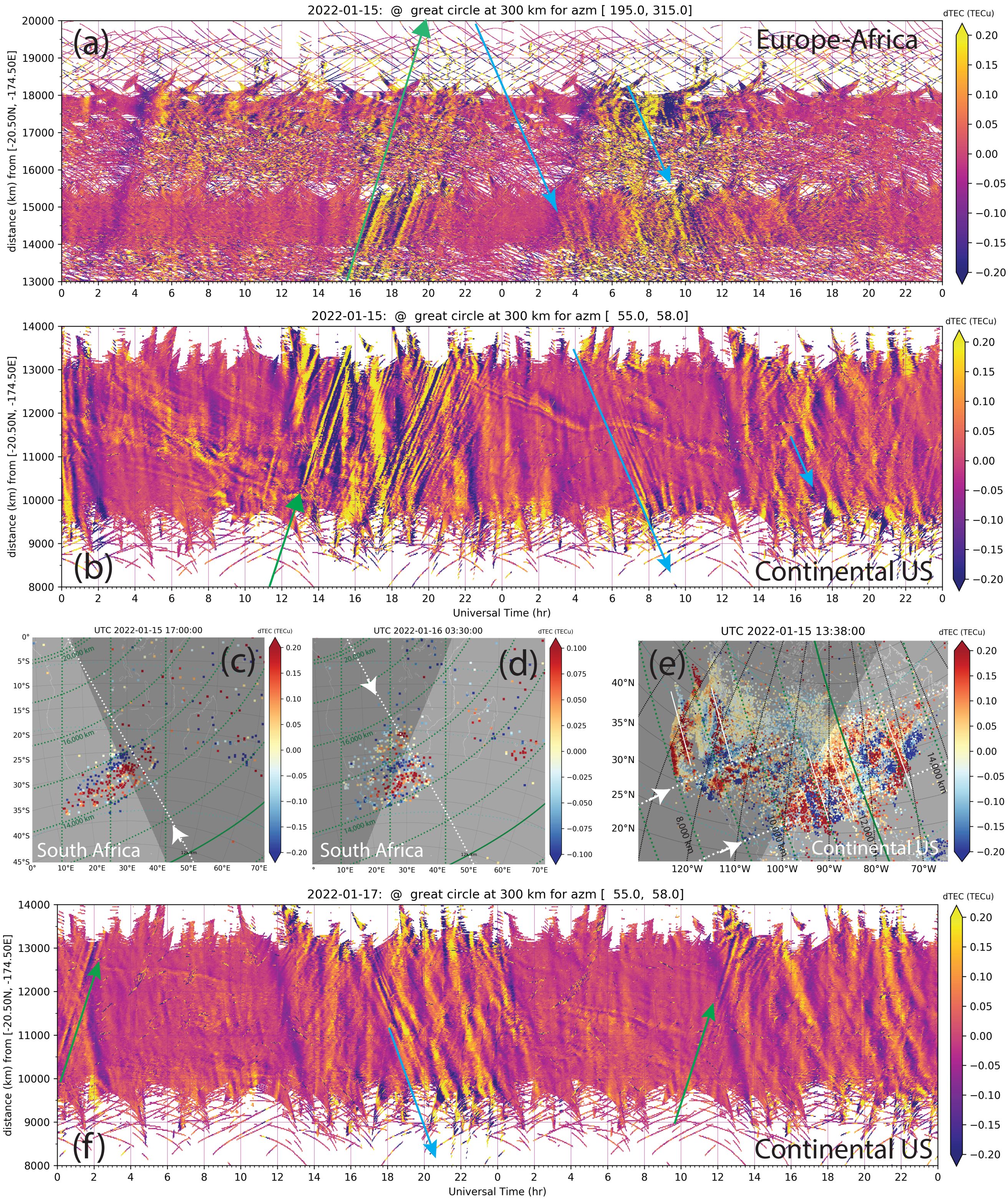

Figure 4. Far-field ionospheric disturbances in selected regions: distance-time variation over Europe-Africa sectors with 195-315°azimuth bearing (a) and the continental US (CONUS) with 55-58°azimuth bearing (b) over 48 hours between 2022-01-15∼16. Green solid lines and arrows mark the radial propagation for outbound waves, at ∼350 m/s (slope); light-blue lines and arrows show the inbound waves toward Tonga on 2022-01-16. (c-d) show TID wavefronts over South Africa corresponding to (a) at 17:00 UT (outbound) and 03:30 UT (inbound). (e) shows TID wavefronts at 13:38 UT over CONUS corresponding to (b), Arrows in (c-e) indicate the radial outbound and inbound propagation along the great circles (marked by white dotted lines). (f) Same as (b) but for 2022-01-17∼18.